

# Gravitational Microlensing Near Caustics I: Folds

B. Scott Gaudi<sup>1,2</sup> and A. O. Petters<sup>3,4</sup>

## ABSTRACT

We study the local behavior of gravitational lensing near fold catastrophes. Using a generic form for the lensing map near a fold, we determine the observable properties of the lensed images, focusing on the case when the individual images are unresolved, i.e., microlensing. Allowing for images not associated with the fold, we derive analytic expressions for the photometric and astrometric behavior near a generic fold caustic. We show how this form reduces to the more familiar linear caustic, which lenses a nearby source into two images which have equal magnification, opposite parity, and are equidistant from the critical curve. In this case, the simplicity and high degree of symmetry allows for the derivation of semi-analytic expressions for the photometric and astrometric deviations in the presence of finite sources with arbitrary surface brightness profiles. We use our results to derive some basic properties of astrometric microlensing near folds, in particular we predict for finite sources with uniform and limb darkening profiles, the detailed shape of the astrometric curve as the source crosses a fold. We find that the astrometric effects of limb darkening will be difficult to detect with the currently planned accuracy of the *Space Interferometry Mission (SIM)* for Galactic bulge sources; however, this also implies that astrometric measurements of other parameters, such as the size of the source, should not be compromised by an unknown amount of limb darkening. We verify our results by numerically calculating the expected astrometric shift for the photometrically well-covered Galactic binary lensing event OGLE-1999-BUL-23, finding excellent agreement with our analytic expressions. Our results can be applied to any lensing system with fold caustics, including Galactic binary lenses and quasar microlensing.

---

<sup>1</sup>School of Natural Sciences, Institute for Advanced Study, Princeton, NJ 08540, gaudi@sns.ias.edu

<sup>2</sup>Hubble fellow

<sup>3</sup>Department of Mathematics, Duke University, Science Drive, Durham, NC 27708, petters@math.duke.edu

<sup>4</sup>Bass Society of Fellows, Duke University

*Subject headings:* astrometry—stars: binaries, fundamental parameters—gravitational lensing

## 1. Introduction

Gravitational lensing has proven to be an exceptional tool for studying a diverse set of astrophysical phenomena. Its utility is due, at least in part, to the fact it operates in a number of qualitatively different regimes. The term strong lensing, or macrolensing, is usually applied when a distant source (typically cosmological) is lensed into multiple, resolved images by an intervening mass, such as a foreground cluster or a galaxy. Weak lensing is used to refer to the case when multiple images are not created, and the gravitational field of the intervening matter serves only to slightly distort the image of the source. For most applications of both strong and weak lensing, the source, lens, and observer can be considered static. The term microlensing is often used to describe the case when multiple images are created, but are not resolved. Typically the separation of the images created by a gravitational microlens are of order the Einstein ring radius,

$$\theta_E = \sqrt{\frac{4GM}{Dc^2}}. \quad (1)$$

Here  $M$  is the mass of the lens,  $D$  is defined by,  $D \equiv D_{os}D_{ol}/D_{ls}$ , and  $D_{os}$ ,  $D_{ol}$ , and  $D_{ls}$  are the distances between the observer-source, observer-lens, and lens-source, respectively. In cosmological contexts, angular diameter distances should be used. When  $\theta_E$  is less than the resolution, individual images in general cannot be distinguished. Due to the small scale of  $\theta_E$ , it is typically not a good approximation to assume that the source, lens, and observer are static. Therefore the lensing properties can be expected to change on timescales of order the Einstein ring crossing time,

$$t_E = \frac{\theta_E D_{ol}}{v_{\perp}}, \quad (2)$$

where  $v_{\perp}$  is the transverse speed of the lens relative to the observer-source line-of-sight. The standard observables in gravitational microlensing are therefore the time rate of change of the total magnification and center-of-light (centroid) of all the microimages. There are two different regimes where microlensing has been discussed: quasar microlensing (Wambsganss 2001) and microlensing in the Local Group (Paczynski 1996).

In the Local Group, gravitational microlensing occurs whenever a massive, compact object passes close to our line of sight to a more distant star. Microlensing was originally suggested as a method to detect baryonic dark matter in the halo of our galaxy (Paczynski 1986), but has been developed and applied as an important tool in studying a number of astrophysical topics, including the stellar mass function (Gould 1996), extrasolar planets

(Mao & Paczyński 1991), stellar atmospheres (Gould 2001), and stellar multiplicity (Alcock et al. 2000; Udalski et al. 2000). The only microlensing effect currently observable is the magnification of the background source as function of time. This is because, for typical distances in the Local Group, the angular Einstein ring radius is  $\theta_E \simeq 1 \text{ mas}(M/M_\odot)^{1/2}$ , and therefore too small to be resolved with current instruments. The timescale for a microlensing event is  $t_E \sim 40$  days. In general, it is much easier to determine the center-of-light of an image than it is to resolve it. Thus future interferometers, such as the *Space Interferometry Mission (SIM)*, although still not able to resolve separations of  $\mathcal{O}(\text{mas})$ , should be able to measure the centroid of all the images to much better than this, perhaps even down to  $10 \mu\text{as}$  in the case of *SIM*. Such accuracy is sufficient to easily detect the motion of the centroid of the images created in a microlensing event, which is also of order  $\theta_E$ . This regime is typically referred to as astrometric microlensing, as opposed to photometric microlensing when only the total magnification is observable.

Astrometric microlensing has a number of important applications. By combining ground-based photometry of microlensing events with photometry and astrometry from an astrometric satellite on an Earth-like orbit, the masses of microlenses can routinely be measured (Paczynski 1998; Boden, Shao & van Buren 1998; Gould & Salim 1999), allowing for the determination of the compact object mass function in the bulge, including stellar remnants (Gould 2000). Astrometric information alone allows for the precise (few %) measurement of the masses of nearby stars (Paczynski 1995). Finally, for a subset of events, it will be possible to obtain precision measurements of angular diameters of stars in the Galactic bulge using astrometric information (Paczynski 1998; Gaudi, Graff, & Han 2002).

Binary microlenses have proven to be enormously useful in photometric microlensing studies. This is primarily because binary lenses exhibit caustics: closed curves on which the mapping from the lens plane to light source plane becomes critical, and the point-source magnification becomes formally infinite. Regions near caustics exhibit large, rapidly changing (with respect to source position) magnification, and are therefore useful not only for providing a large source flux, but also high angular resolution. However, binary lenses have also proven to be difficult to study both theoretically and observationally. This is partially because the lens equation, which describes the mapping from the lens plane to the light source plane, is equivalent to a fifth-order complex polynomial in the source position (Witt 1990), and therefore is not analytically solvable in general. Furthermore, care must be taken when considering finite source effects near caustics due to the divergent magnification. However, considerable progress can be made when one realizes that the smooth arcs (away from cusps) of caustics that arise in nearly equal-mass binary lenses are well approximated as simple linear fold catastrophes, which have generic, simple, and most importantly, *analytic* behavior. Thus the caustics of binary lenses can be analyzed analytically or semi-analytically

without reference to the global (and non-analytic) topology of the general binary lens. In particular, a simple equation for the magnification of a source near a fold exists (Schneider et al. 1992), which has been used in a number of important applications including binary-lens fitting (Albrow et al. 1999), stellar atmospheres (Gaudi & Gould 1999), and caustic-crossing predictions (Jaroszyński & Mao 2001).

In contrast to the astrometric behavior of single lenses, which is analytic and has been quite well studied (Walker 1995; Jeong, Han & Park 1999), there have been only a few preliminary studies of the astrometric properties of binary gravitational lenses (Han, Chun, & Chang 1999; Chang & Han 1999; Gould & Han 2000). It is known that astrometric binary-lens curves exhibit complex behavior, including instantaneous  $\mathcal{O}(\theta_E)$  jumps in the image centroid trajectory that occur when a point source crosses a binary-lens caustic and two highly-magnified images appear in a position unrelated to the position of the centroid of the other three binary-lens images. The generic behavior of these centroid jumps, or how they are altered by finite source effects, is not understood. As is the case for photometric microlensing, the astrometric behavior of binary lenses will likely prove quite useful for several applications. The usefulness of binary lenses is primarily related to the complex image centroid trajectories and the large centroid jumps. Although, in general, these properties do not allow one to measure any additional parameters over the single lens case; they do allow one to measure these parameters much more easily. In particular, Graff & Gould (2002) have shown that lens mass measurements can be made to a given accuracy with 1-3 orders of magnitude fewer photons with caustic-crossing binary-lens events than with single lens events, thus greatly reducing the resources required to achieve one of the primary proposed science goals of astrometric microlensing. Caustic crossing binary-lens events are also enormously useful for measuring the angular radii of microlensing source stars in the bulge, for two reasons. First, the expected ratio of binary-to-single lens events for which the source star is resolved is a factor of  $\gtrsim 4$  for giant sources and  $\gtrsim 10$  for main sequence sources. Furthermore, the large and complex centroid shifts expected for caustic-crossing binary-lens events makes the requisite astrometric measurements easier. Gaudi, Graff, & Han (2002) have shown that, by combining accurate ground-based photometry with a handful of precise astrometric measurements, caustic-crossing binary-lens events should yield  $\sim 5\%$  stellar radius measurements with reasonable expenditure of resources.<sup>5</sup> Thus, given the importance of caustic crossing binary-lens events, an analytic study of the generic behavior of astrometric microlensing near folds would prove quite useful.

In quasar microlensing, the separate macroimages of a quasar that is multiply-imaged

---

<sup>5</sup>Although it is possible to measure stellar angular sizes using astrometric information alone, this generally requires very densely-sampled measurements, since the source is resolved only for a short time.

by a intervening galaxy or cluster also feel the combined, non-linear effect of individual point masses (i.e. stars) in the macrolensing object that are near the macroimage position. The individual macroimages are in fact composed of many, unresolved microimages with separations of order the Einstein radius of a  $M \sim M_\odot$  object at cosmological distances,  $\theta_E \simeq 1\mu\text{as}(M/M_\odot)^{1/2}$ . The typical timescale for the source to cross an angle of  $\theta_E$  is  $t_E \simeq 15$  years; however microlensing light curves should show structure on much smaller timescales due to the combined effects of many individual microlenses. Since it was first discussed by Chang & Refsdal (1979), cosmological microlensing has been studied theoretically by numerous authors (see Wambsganss 2001 and references therein), and detected in at least two systems (Q2237+0305, Irwin et al. 1989; Corrigan et al. 1991; Woźniak et al. 2000, B1600+434, Koopmans & de Bruyn 2000). Observations have been used to place constraints on, e.g., the size of the emitting region of quasars (Wambsganss, Schneider, & Paczynski 1990; Wyithe, Webster, Turner, & Mortlock 2000) and the mass function of microlenses (Schmidt & Wambsganss 1998; Wyithe, Webster, & Turner 2000; Koopmans & de Bruyn 2000).

Quasar microlensing differs markedly from microlensing in the Local Group in that the surface mass density in units of the critical density for lensing (the “optical depth”) is of order unity, rather than  $\mathcal{O}(10^{-6})$  for the Local Group. In the high optical depth regime the lensing effects of the individual microlenses add nonlinearly, resulting in a complex caustic network. Due to this nonlinear behavior and the large number of lenses typically involved, calculation of the observable properties of such a lensing system is difficult and time consuming. Although in the high optical depth regime the caustics often exhibit considerably more complicated global behavior than the caustics of binary lenses in the Local Group, it is still the case that the smooth arcs (away from cusps) of the caustics are locally well-approximated by generic fold catastrophes. This fact, combined with a simple formula for the magnification near folds, has been exploited by numerous authors to quickly and efficiently calculate various observable properties of quasar microlensing (Wambsganss & Paczynski 1991; Lewis & Ibata 1998; Wyithe & Webster 1999; Fluke & Webster 1999).

The observable effects of quasar microlensing have been limited to the relative magnifications of the various macroimages as a function of time. As with Local Group microlensing, astrometric effects should also be present. The centroid of the individual macroimages should vary as a function of time, particularly when new images are created or destroyed when the source crosses a caustic. This effect has been studied by Williams & Saha (1995) and Lewis & Ibata (1998). In particular, Lewis & Ibata (1998) predict that magnitude of the centroid shift for the Q2237+0305 system (apparent magnitude  $R \lesssim 18.5$ ) can be as large as  $\sim 50\mu\text{as}$ , and thus potentially observable with *SIM*. They also note that the magnitude of the centroid shift is often correlated with the magnitude of the change in total magnification. The analytic results presented in this paper may prove useful for this application.

Here we study the generic, local behavior of microlensing near fold catastrophes. In §2 we present an analytic study of the photometric and astrometric behavior near folds. We begin with the equations that describe the mapping near a fold caustic in §2.1, and use these to derive the behavior of a point source near a fold. We extend this analysis to finite sources in §2.2, and limb-darkened sources in §2.3. In §2.4 we show how and when our generic parabolic fold form reduces to the more familiar linear caustic. In §2.5 we use our analytic results to derive some generic results about the astrometric behavior near folds. We verify the applicability of our results in §3 by numerically calculating the photometric and astrometric behavior of one well-observed binary-lens event. We find excellent agreement with our analytic formulae. Finally, we summarize and conclude in §4.

Our goal is to provide a thorough, comprehensive study of gravitational microlensing near fold caustics. Although our study is interesting in its own right, the primary utility of the results presented here is their potential application to the topics mentioned in the previous paragraphs. A prescription for how specifically our results can be applied to these topics is beyond the scope of this paper, but we will make general comments along these lines over the course of the paper, and more specific comments in §2.5. We are currently preparing a complementary, similarly detailed study of microlensing near cusps. Combined with this study, we will have a reasonably thorough and complete understanding of the local behavior of microlensing observables near all stable gravitational lensing singularities. We note that some of the results derived here, particularly the results on the photometric behavior near folds, have been presented elsewhere (see, e.g. Schneider et al. 1992, Petters et al. 2001, and Fluke & Webster 1999). We include those results here for the sake of completeness.

## 2. Analytic Considerations

### 2.1. Lensing Near Fold Caustics

#### 2.1.1. Global Lensing Map

For a general gravitational lens, the lensed images  $\boldsymbol{\theta}$  of a source  $\boldsymbol{u}$ , are given by the solutions of the lens equation, which is the mapping  $\boldsymbol{u} \rightarrow \boldsymbol{\theta}$ :

$$\boldsymbol{u} = \boldsymbol{\eta}(\boldsymbol{\theta}) \equiv \boldsymbol{\theta} - \boldsymbol{\alpha}(\boldsymbol{\theta}), \quad (3)$$

where  $\boldsymbol{\alpha} = \nabla\psi$ , and  $\psi$  is the projected Newtonian potential of the lens,

$$\psi(\boldsymbol{\theta}) = \frac{1}{\pi} \int_{\mathbb{R}^2} d\boldsymbol{\theta}' \kappa(\boldsymbol{\theta}') \ln |\boldsymbol{\theta} - \boldsymbol{\theta}'|. \quad (4)$$

Where  $\kappa = \Sigma(\boldsymbol{\theta})/\Sigma_{cr}$ ,  $\Sigma(\boldsymbol{\theta})$  is the surface density of the lens, and

$$\Sigma_{cr} \equiv \frac{c^2}{4\pi G} \frac{D_{os}}{D_{ol}D_{ls}} \quad (5)$$

is the critical surface density for lensing. Note that  $\nabla^2\psi = 2\kappa$ . We are assuming that  $\boldsymbol{\theta} = \mathbf{r}/(\theta_E D_{ol})$  and  $\mathbf{u} = \mathbf{s}/(\theta_E D_{os})$ , where  $\mathbf{r}$  and  $\mathbf{s}$  are the proper vector positions in the lens and light source planes, respectively. The mapping  $\boldsymbol{\eta}$  can produce multiple images of the source  $\mathbf{u}$ . The magnification of lensed image  $\boldsymbol{\theta}_i$  is

$$\mu(\boldsymbol{\theta}_i) = \frac{1}{|\det[A\boldsymbol{\eta}(\boldsymbol{\theta}_i)]|}, \quad (6)$$

where  $A\boldsymbol{\eta}$  is the Jacobian matrix of the lensing map  $\boldsymbol{\eta}$ . The critical curve is the set of positions  $\boldsymbol{\theta}_c$  such that the determinant of the Jacobian matrix vanishes, i.e. where

$$J \equiv \det[A\boldsymbol{\eta}(\boldsymbol{\theta}_c)] = 0, \quad (7)$$

and the caustics are  $\mathbf{u}_c = \boldsymbol{\eta}(\boldsymbol{\theta}_c)$ . In the case of microlensing, the individual images are by definition unresolved, and thus it is useful to define the total magnification

$$\mu_{tot} = \sum_i \mu(\boldsymbol{\theta}_i), \quad (8)$$

where the sum is over all images. The center-of-light, or centroid  $\boldsymbol{\theta}_{cl}(\mathbf{u})$  of the images is simply the magnification weighted sum of the image positions,

$$\boldsymbol{\theta}_{cl}(\mathbf{u}) = \frac{\sum_i \mu(\boldsymbol{\theta}_i) \boldsymbol{\theta}_i}{\mu_{tot}}. \quad (9)$$

For simplicity, we will focus primarily on the quantity  $\boldsymbol{\theta}_{cl}$ . However, it is important to note that, in general, centroid measurements will be made with respect to the unlensed source position, thus the observable is

$$\delta\boldsymbol{\theta}_{cl}(\mathbf{u}) = \boldsymbol{\theta}_{cl}(\mathbf{u}) - \mathbf{u}. \quad (10)$$

Also, while the angular variables we will be working with will be in units of  $\theta_E$ , the astrometric observables are in physical units, such as arcseconds. To convert to observable quantities, all angular quantities must be multiplied by  $\theta_E$ . For example, the observable centroid shift is given by  $\delta\boldsymbol{\varphi}_{cl} \equiv \theta_E \delta\boldsymbol{\theta}_{cl}$ .

### 2.1.2. Lensing Map Near Folds

We now derive the generic behavior of the photometric and astrometric properties of gravitational lensing near folds. We will present our derivations in some detail, in order to document the approximations and simplifying assumptions that are implicit in the final analytic expressions. In Figure 1, we provide an illustrative example of the basic properties of lensing near a fold. We will refer to this figure repeatedly during the course of the derivations.

Suppose that the lensing map  $\boldsymbol{\eta}$  sends the origin to itself (which can always be accomplished by appropriate translations) and a fold caustic curve passes through the origin. By Taylor expanding the gravitational potential  $\psi$  about the origin, one can find an orthogonal change of coordinates that is the same in the lens and light source planes such that the lensing map  $\boldsymbol{\eta}$  can be approximated by the following mapping in a neighborhood of the origin (Petters, Levine, & Wambsganss 2001, pp. 341-353; Schneider, Ehlers, & Falco 1992, p. 187):

$$u_1 = a\theta_1 + \frac{b}{2}\theta_2^2 + c\theta_1\theta_2, \quad u_2 = \frac{c}{2}\theta_1^2 + b\theta_1\theta_2 + \frac{d}{2}\theta_2^2, \quad (11)$$

where  $(\theta_1, \theta_2)$  and  $(u_1, u_2)$  denote the respective coordinates in the lens and light source planes, and

$$a = 1 - \psi_{11}(\mathbf{0}) \neq 0, \quad b = -\psi_{122}(\mathbf{0}), \quad c = -\psi_{112}(\mathbf{0}), \quad d = -\psi_{222}(\mathbf{0}) \neq 0. \quad (12)$$

Here the subscripts refer to the partial derivatives of  $\psi$  with respect to the original global Cartesian coordinates of the lensing map. For the example in Figure 1, we have adopted  $a = 5$ ,  $b = 1$ , and  $c = -d = -0.5$ .

The Jacobian matrix of equation (11) is

$$A = \begin{bmatrix} a + c\theta_2 & c\theta_1 + b\theta_2 \\ c\theta_1 + b\theta_2 & b\theta_1 + d\theta_2 \end{bmatrix}. \quad (13)$$

The critical curve is given by

$$J \equiv \det A = (a + c\theta_2)(b\theta_1 + d\theta_2) - (c\theta_1 + b\theta_2)^2 = 0. \quad (14)$$

The tangent line to the critical curve at the origin is given by

$$0 = \boldsymbol{\theta} \cdot \nabla J(\mathbf{0}) = ab\theta_1 + ad\theta_2, \quad (15)$$

that is,

$$\theta_2 = -\frac{b}{d}\theta_1 \quad (16)$$



since  $a \neq 0$  and  $d \neq 0$ . Substituting  $\theta_2 = -b\theta_1/d$  into equation (11) yields

$$u_1 = a\theta_1 + \frac{b}{d^2} \left( \frac{1}{2}b^2 - cd \right) \theta_1^2 \simeq a\theta_1, \quad u_2 = \frac{1}{2d}(cd - b^2) \theta_1^2. \quad (17)$$

Note that in the expression for  $u_1$ , the term  $\theta_1$  dominates  $\theta_1^2$  near the origin. Inserting  $\theta_1 = u_1/a$  into  $u_2$  above, we see that the tangent line at the origin of the critical curve is mapped into a parabola (Schneider et al. 1992; Fluke & Webster 1999):

$$C(u_1, u_2) \equiv 2a^2d(u_2 - eu_1^2) = 0. \quad (18)$$

where we have introduced the combination of local derivatives of  $\psi$ :

$$e \equiv \frac{cd - b^2}{2a^2d}. \quad (19)$$

We show in §2.4 that  $|e|$  is one-half the curvature of the caustic at the origin. Thus when  $|e| \ll 1$ , the caustic can be approximated as  $2a^2du_2 = 0$ , i.e. the  $u_1$ -axis. For the example shown in Figure 1,  $|e| = 0.05$ .

Since the tangent line (Eq. 16) approximates the critical curve near the origin, the parabola (Eq. 18) approximates the caustic near the origin. See Figure 1(a,b). Now multiplying  $u_2$  in equation (11) by  $2a^2$  and substituting  $\theta_1 = u_1/a$  yields

$$C(u_1, u_2) = (b u_1 + ad \theta_2)^2. \quad (20)$$

Hence, if a light source is located at a position  $(u_1, u_2)$  where  $C(u_1, u_2) < 0$ , then there is no lensed image locally, while a source with  $C(u_1, u_2) \geq 0$  has at least one image.

For an  $n$ -point mass lens, we have  $c = -d$ . Consequently, if  $d > 0$ , the parabolic caustic lies in the lower-half plane locally. In addition, the region above the parabola is such that sources lying there have double images locally (Fig. 1a). If  $d < 0$ , then parabola is in the upper-half plane with the region below the parabola yielding double images locally. In other words, the caustic is locally convex (see Petters et al. 2001, Sec 9.3 for a detailed treatment).

### 2.1.3. Image Positions of Sources Near Folds

Let us determine the images for  $C(u_1, u_2) \geq 0$ . Equation (20) is equivalent to a quadratic equation in  $\theta_2$ ,

$$0 = [a^2d^2] \theta_2^2 + [2abdu_1] \theta_2 + [b^2u_1^2 - C(u_1, u_2)]. \quad (21)$$

The solutions are<sup>6</sup>

$$\theta_2 = \frac{-bu_1 \pm \sqrt{C(u_1, u_2)}}{ad}. \quad (22)$$

The expression for  $u_1$  in equation (11) yields

$$\theta_1 = \frac{1}{a + c\theta_2} \left( u_1 - \frac{b}{2}\theta_2^2 \right). \quad (23)$$

Ignoring terms of order 3 or higher, we obtain

$$\theta_1 = \frac{u_1}{a} - \frac{c}{a^2}u_1\theta_2 - \frac{b}{2a}\theta_2^2, \quad (24)$$

where the approximation  $(a + c\theta_2)^{-1} \simeq a^{-1}(1 - c\theta_2/a)$  was employed. Substituting equation (22) into (24) and keeping only terms that are linear in  $u_1$  and  $u_2$ , it follows that

$$\theta_1 = \frac{du_1 - bu_2}{ad}. \quad (25)$$

Hence, a source with  $C(u_1, u_2) > 0$  has two (opposite parity) images given by

$$\boldsymbol{\theta}_{\pm} \equiv (\theta_{\pm,1}, \theta_{\pm,2}) = \frac{1}{ad} \left( du_1 - bu_2, -bu_1 \pm \sqrt{C(u_1, u_2)} \right). \quad (26)$$

Figure 1(a,b) illustrates the mapping from source to images near a fold.

Consider a point  $\mathbf{u}_c$  on the caustic, i.e.,  $C(\mathbf{u}_c) = 0$ . Locally there is one image of  $\mathbf{u}_c$ , located on the critical curve<sup>7</sup> at the position

$$\boldsymbol{\theta}_c = \frac{1}{ad} (du_{c,1} - bu_{c,2}, -bu_{c,1}). \quad (27)$$

Now consider a source at  $\mathbf{u} = (u_1, u_2)$  inside the caustic (i.e.,  $C(\mathbf{u}) > 0$ ) and let  $\mathbf{u}_c^* = (u_{c,1}^*, u_{c,2}^*)$  be the point on the caustic with the same horizontal position as  $\mathbf{u}$ , i.e.,  $u_{c,1}^* = u_1$  and  $u_{c,2}^* \neq u_2$ . The vertical separation of the source from the caustic is then the difference between the  $u_2$ -coordinates of  $\mathbf{u}$  and  $\mathbf{u}_c^*$ :

$$\Delta u_{2,\perp} \equiv u_2 - e(u_{c,1}^*)^2 = \frac{C(u_1, u_2)}{2a^2d}. \quad (28)$$

---

<sup>6</sup>Note that we do not need to include  $\text{sign}(ad)$  in front of the square root since  $\pm \text{sign}(ad) = \pm 1$ .

<sup>7</sup>That the image position in equation (27) corresponds to a point on the critical curve can be seen by noting that on the caustic  $u_{c,2} = eu_{c,1}^2$ , and close to the origin,  $u_1$  dominates  $u_2$ , and thus the image position is  $\boldsymbol{\theta}_c = (du_{c,1}, -bu_{c,1})/(ad)$ , which is indeed a point on the critical line (see Eq. 16).

Note that  $\Delta u_{2,\perp} > 0$  if and only if  $d > 0$  (since the source is located where  $C(u_1, u_2) > 0$ ). Using equations (26) and (27), we find that the distances of the images  $\boldsymbol{\theta}_\pm(u_1, u_2)$  from the point  $\boldsymbol{\theta}_c$  on the critical line are the same,

$$\Delta\theta_{2,\perp} = |\boldsymbol{\theta}_\pm(u_1, u_2) - \boldsymbol{\theta}_c| = \sqrt{\frac{2\Delta u_{2,\perp}}{d}} \left[ 1 + \frac{b^2}{2a^2d} \Delta u_{2,\perp} \right]^{1/2}. \quad (29)$$

Near the origin, the first term in brackets dominates over the second, and thus,

$$\Delta\theta_{2,\perp} = \sqrt{\frac{2\Delta u_{2,\perp}}{d}}. \quad (30)$$

#### 2.1.4. Magnification of Sources Near Folds

Using the earlier tangent line approximation to the critical curve at the origin, we Taylor expand the Jacobian determinant  $J$  about the origin to first order:

$$J(\theta_1, \theta_2) = J_{\theta_1}(\mathbf{0})\theta_1 + J_{\theta_2}(\mathbf{0})\theta_2 = ab \theta_1 + ad \theta_2, \quad (31)$$

which is equal to the right-hand-side of (15). Inserting the expressions for  $\theta_1$  and  $\theta_2$  from equation (26), we obtain

$$J(\theta_1, \theta_2) = -\frac{b^2}{d}u_2 \pm \sqrt{C(u_1, u_2)}. \quad (32)$$

Keeping only the lowest order terms in  $u_1$  and  $u_2$  gives,

$$|J(\boldsymbol{\theta}_\pm)| = \sqrt{C(u_1, u_2)}. \quad (33)$$

In terms of the vertical separation between the source and the caustic (Eq. 28), the magnification of the images are given locally by

$$\mu_\pm \equiv \mu(\boldsymbol{\theta}_\pm) = \frac{1}{|J(\boldsymbol{\theta}_\pm)|} = \frac{1}{2} \sqrt{\frac{u_f}{\Delta u_{2,\perp}}}, \quad (34)$$

where  $u_f = 2/(a^2d)$ . Thus the two images have the same magnification if the source is sufficiently close to the caustic. The total magnification  $\mu_f \equiv 2\mu_\pm$  of the two images is simply

$$\mu_f = \sqrt{\frac{u_f}{\Delta u_{2,\perp}}}, \quad (35)$$

which agrees with the expressions derived by both Schneider, Ehlers & Falco (1992, p190) and Fluke & Webster (1999). Equation (35) is the well-known result that the magnification varies inversely as the square-root of the distance of the source from the caustic. It is not

often appreciated however, that this property holds for the general parabolic fold form as well, provided that the *vertical distance* is used, rather than, for example, the minimum distance between the source and the fold caustic. Rigorously, the vertical distance is the distance between the source and the caustic in the direction perpendicular to the tangent line of the caustic at the origin, where the origin is defined as the point around which the potential  $\psi$  is Taylor expanded. In the limit of a straight fold ( $|e| \ll 1$ ), the vertical distance and the minimum distance are equivalent.

### 2.1.5. Image Centroid of Sources Near Folds

Write the source position  $\mathbf{u}$  in terms of the fold local coordinates, i.e.,  $\mathbf{u} = (u_1, u_2)$ . There are no local images for source a position with  $C(\mathbf{u}) < 0$ . From equations (9) and (26), and since  $\mu_+ = \mu_-$ , for sources inside the caustic the centroid is given locally as

$$\boldsymbol{\theta}_f(\mathbf{u}) = \frac{1}{2}(\boldsymbol{\theta}_+ + \boldsymbol{\theta}_-) = \frac{1}{ad}(du_1 - bu_2, -bu_1), \quad \text{for } C(\mathbf{u}) \geq 0. \quad (36)$$

We express the rectilinear motion of the source as follows:

$$\mathbf{u}(t) = \mathbf{u}_c + (t - t_c)\dot{\mathbf{u}}, \quad (37)$$

where  $\mathbf{u}_c$  is the position at which the source intersects the caustic at time  $t = t_c$  and  $\dot{\mathbf{u}}$  is the constant angular velocity vector of the source,

$$\dot{\mathbf{u}} = \left( \frac{\cos \phi}{t_E}, \frac{\sin \phi}{t_E} \right). \quad (38)$$

Recall that  $t_E = \theta_E D_{ol}/v_\perp$ , where  $v_\perp$  is the transverse speed of the lens relative to the observer-source line-of-sight. Here  $\phi$  is the angle of the source's trajectory with respect to the  $u_1$ -axis. Note that the  $u_1$ -axis does not necessarily coincide with the caustic, and thus  $\phi$  is not necessarily the angle of the trajectory with respect to the tangent to the caustic at  $\mathbf{u}_c$ .

We shall assume that  $t > t_c$  corresponds to the source's trajectory lying in the double-image region. In that region, the centroid follows a straight line locally:

$$\boldsymbol{\theta}_f(t) = \boldsymbol{\theta}_{f,c} + (t - t_c)\dot{\boldsymbol{\theta}}_{(f,c)}, \quad \text{for } t \geq t_c \quad (39)$$

where  $\boldsymbol{\theta}_{f,c} \equiv \boldsymbol{\theta}_f(\mathbf{u}_c)$  and  $\dot{\boldsymbol{\theta}}_{(f,c)} \equiv d\boldsymbol{\theta}_f/dt|_{t=t_c} = \boldsymbol{\theta}_f(\dot{\mathbf{u}})$  (both constant vectors). Note that since the slope of the centroid line  $\boldsymbol{\theta}_f$  is,  $\tan \phi_c = (-b \cos \phi)/(d \cos \phi - b \sin \phi)$ , where  $\phi_c$  is the angle between the centroid line and the  $\theta_1$ -axis, it follows that  $\dot{\boldsymbol{\theta}}_{(f,c)}$  can be expressed as

$$\dot{\boldsymbol{\theta}}_{(f,c)} = \frac{-b \cos \phi}{ad t_E}(\cot \phi_c, 1). \quad (40)$$

### 2.1.6. Global Magnification and Centroid

Fold caustics do not, of course, exist in isolation. They are tied to the global properties of the lens in consideration. For practical purposes, we therefore consider images created by the lens that are not associated with the fold under consideration. We define  $\mu_0$  to be the total magnification of all the images not associated with the fold, and we define  $\boldsymbol{\theta}_0$  as the centroid of all these images. We will assume that there is locally only one fold caustic, and that all the other image magnifications and positions are only slowly varying functions of the source position. The total magnification is then

$$\mu_{tot} = \mu_f + \mu_0 = \left( \frac{u_f}{\Delta u_{2,\perp}} \right)^{1/2} \Theta(\Delta u_{2,\perp}) + \mu_0. \quad (41)$$

See Figure 1(c). Here  $\Theta$  is the Heaviside unit step function (i.e.,  $\Theta(x) = 1$  for  $x \geq 0$  and  $\Theta(x) = 0$  if  $x < 0$ ); it accounts for the fact that sources below the caustic (with  $\Delta u_{2,\perp} < 0$ ) have no images locally (i.e., near the critical curve). Since  $\mu_+ = \mu_- = \mu_f/2$ , we have,

$$\boldsymbol{\theta}_{cl} = \frac{1}{\mu_{tot}} [\mu_f \boldsymbol{\theta}_f + \mu_0 \boldsymbol{\theta}_0] \quad (42)$$

where

$$\boldsymbol{\theta}_f(\mathbf{u}) = \frac{1}{ad} (du_1 - bu_2, -bu_1) \Theta(\Delta u_{2,\perp}). \quad (43)$$

We can calculate the dependence of the observables  $\mu_{tot}$  and  $\boldsymbol{\theta}_{cl}$  on time by assuming a rectilinear source trajectory and replacing  $\mathbf{u}$  in equations (41) and (42) by equation (37). We first Taylor expand  $\boldsymbol{\theta}_0$  and  $\mu_0$  about the time of the caustic crossing,  $t = t_c$ , keeping terms of first order in  $t - t_c$ :

$$\boldsymbol{\theta}_0 = \boldsymbol{\theta}_{0,c} + (t - t_c) \dot{\boldsymbol{\theta}}_{(0,c)}, \quad (44)$$

$$\mu_0 = \mu_{0,c} + (t - t_c) \dot{\mu}_{(0,c)}, \quad (45)$$

where  $\dot{\boldsymbol{\theta}}_{(0,c)} \equiv d\boldsymbol{\theta}_0/dt|_{t=t_c}$  and  $\dot{\mu}_{(0,c)} \equiv d\mu_0/dt|_{t=t_c}$ . From equations (28) and (37),  $\Delta u_{2,\perp}$  is given by

$$\Delta u_{2,\perp} = \frac{t - t_c}{t_E} \sin \phi \left[ 1 - e \cot \phi \left( 2u_{c,1} + \frac{t - t_c}{t_E} \cos \phi \right) \right]. \quad (46)$$

The magnification as a function of time is then,

$$\begin{aligned} \mu_{tot}(t) = & \left( \frac{t_f}{t - t_c} \right)^{1/2} \left[ 1 - e \cot \phi \left( 2u_{c,1} + \frac{t - t_c}{t_f} u_f \cot \phi \right) \right]^{-1/2} \Theta(t - t_c) \\ & + \mu_{0,c} + \dot{\mu}_{(0,c)}(t - t_c), \end{aligned} \quad (47)$$

where  $t_f \equiv (u_f t_E)/\sin \phi$  is the effective rise time of the caustic crossing, and  $u_f = 2/(a^2 d)$  defines the characteristic rise length as before. Notice that when the curvature of the caustic is small, i.e., when  $|e| \ll 1$ , the magnification associated with the fold reduces to the more familiar form  $\mu_f = [(t - t_c)/t_f]^{-1/2} \Theta(t - t_c)$ . The centroid of all images is

$$\boldsymbol{\theta}_{cl}(t) = \frac{1}{\mu_{tot}} \left\{ [\mu_f \boldsymbol{\theta}_{f,c} \Theta(t - t_c) + \mu_0 \boldsymbol{\theta}_{0,c}] + [\mu_f \dot{\boldsymbol{\theta}}_{(f,c)} \Theta(t - t_c) + \mu_0 \dot{\boldsymbol{\theta}}_{0,c}] (t - t_c) \right\}, \quad (48)$$

where  $\boldsymbol{\theta}_{f,c}$  and  $\dot{\boldsymbol{\theta}}_{(f,c)}$  are defined below equation (39). Figure 1(e,f) illustrates the behavior of the two components of  $\boldsymbol{\theta}_{cl}(t)$  as a function of time, whereas Figure 1(g) shows  $\theta_{cl,1}$  versus  $\theta_{cl,2}$ .

## 2.2. Finite Sources

### 2.2.1. Finite Source Magnification

The results of the previous section assumed a pointlike source. This results in an astrometric curve that exhibits an instantaneous jump from  $\boldsymbol{\theta}_{0,c}$  to  $\boldsymbol{\theta}_{f,c}$  at  $t = t_c$ . All real sources will have a finite extent which will smooth out the discontinuous jump. For a finite source, the magnification is the surface brightness weighted magnification integrated over the area of the source,

$$\mu^{fs} = \frac{\int_D d\mathbf{u} S(\mathbf{u}) \mu(\mathbf{u})}{\int_D d\mathbf{u} S(\mathbf{u})}, \quad (49)$$

where  $D$  is the disc-shaped region of the source and  $S(\mathbf{u})$  is the surface brightness of the source. Let  $\bar{S}$  be the average surface brightness of the source,  $\bar{S} \equiv (\pi \rho_*^2)^{-1} \int_D d\mathbf{u} S(\mathbf{u})$ . Here  $\rho_* \equiv \theta_*/\theta_E$ , is the angular source radius  $\theta_*$  in units of  $\theta_E$ . The denominator in equation (49) is then simply  $\pi \rho_*^2 \bar{S}$ . Define  $S_N \equiv S(\mathbf{u})/\bar{S}$  to be the normalized surface brightness. Also define a new set of source plane coordinates such that

$$\mathbf{u}' = \frac{\mathbf{u} - \mathbf{u}_{cn}}{\rho_*}, \quad (50)$$

where  $\mathbf{u}_{cn}$  is the position of the center of the source. Then for a point  $\mathbf{u}$  inside the disc source  $D$ , we have  $|\mathbf{u}'| \leq 1$ . Equation (49) becomes

$$\mu^{fs} = \frac{1}{\pi} \int_D d\mathbf{u}' S_N(\mathbf{u}') \mu(\mathbf{u}'). \quad (51)$$

All of the preceding results apply to generic parabolic fold catastrophes. However, in order to continue making significant progress analytically, we must make the following simplifying assumption: We furthermore assume that  $|e| \ll 1$ , and thus the caustic coincides with

the  $u_1$ -axis and  $\Delta u_{2,\perp} = u_2$ . This considerably simplifies the form for the fold magnification  $\mu_f$ .

Let  $z$  be such that  $z\rho_*$  is the vertical separation of the center  $\mathbf{u}_{cn}$  of the source from the caustic, i.e.,  $u_{cn,2} = z\rho_*$ . The source  $D$  is in the upper-half plane (i.e.,  $u_2 \geq 0$ ) if and only if  $z \geq 1$ . If  $z = 1$ , then  $D$  just touches the caustic, while for  $0 < z < 1$  a portion of  $D$  is below the caustic with the center of  $D$  on the caustic for  $z = 0$ . The center of  $D$  lies below the caustic for  $z < 0$ , with a portion of  $D$  still above the caustic for  $-1 < z < 0$  and  $D$  completely below the caustic for  $z < -1$ . Since the fold magnification  $\mu_f$  is nonzero only for points  $\mathbf{u}$  in  $D$  that lie in the upper-half plane, we get

$$\mu_f(\mathbf{u}') = \left(\frac{u_f}{\rho_*}\right)^{1/2} \frac{\Theta(1+z)}{\sqrt{u'_2+z}}. \quad (52)$$

By equations (51) and (52), we find for a fold caustic and arbitrary surface brightness profile,

$$\mu_f^{fs}(z) = \left(\frac{u_f}{\rho_*}\right)^{1/2} \left[ \frac{1}{\pi} \int_{\max(-z,-1)}^1 du'_2 \frac{\Theta(1+z)}{\sqrt{u'_2+z}} \int_{-\sqrt{1-(u'_2)^2}}^{\sqrt{1-(u'_2)^2}} du'_1 S_N(u'_1, u'_2) \right]. \quad (53)$$

For a uniform source, i.e.,  $S_N(\mathbf{u}') = 1$ , this simplifies to (Schneider et al. 1992; Albrow et al. 1999),

$$\mu_f^{us}(z) = \left(\frac{u_f}{\rho_*}\right)^{1/2} G_0(z), \quad (54)$$

where

$$G_n(z) \equiv \pi^{-1/2} \frac{(n+1)!}{(n+1/2)!} \int_{\max(-z,-1)}^1 dx \frac{(1-x^2)^{n+1/2}}{(x+z)^{1/2}} \Theta(1+z). \quad (55)$$

Note that  $G_0$  can be expressed as an elliptic integral. Figure 2 shows  $G_0(z)$  for  $-2 \leq z \leq 2$ . For small source sizes  $\theta_* \ll \theta_E$ , the magnification  $\mu_0$  of the images not associated with fold is a slowly varying function of  $\mathbf{u}$  over the source, and thus  $\pi^{-1} \int_D d\mathbf{u}' S_N(\mathbf{u}') \mu_0(\mathbf{u}') = \mu_0(\mathbf{u}_{cn})$ . Therefore, the total finite source magnification is just

$$\mu_{tot}^{us} = \mu_f^{us} + \mu_{0,cn}, \quad (56)$$

where  $\mu_{0,cn} \equiv \mu_0(\mathbf{u}_{cn})$ . In analogy to the point source case (§2.1), we can expand  $\mu_0$  about the time of the second caustic crossing. For a source with rectilinear motion, the total finite source magnification in the time domain is then,

$$\mu_{tot}^{us}(t) = \left(\frac{t_f}{\Delta t}\right)^{1/2} G_0\left(\frac{t-t_c}{\Delta t}\right) + \mu_{0,c} + \dot{\mu}_{(0,c)}(t-t_c), \quad (57)$$

where  $t_f \equiv (u_f t_E)/\sin \phi$  (effective rise time of the caustic crossing) and  $\Delta t \equiv (\rho_* t_E)/\sin \phi$  is the time scale of the caustic crossing, i.e., the time between when the source first touches the caustic and when it straddles the caustic. Note that  $t_f/\Delta t = u_f/\rho_*$ . Figure 1(d) illustrates the behavior of  $\mu_{tot}^{us}(t)$ .

### 2.2.2. Finite Source Image Centroid

For an extended source, the image centroid is the position of the images weighted by both the surface brightness and magnification, integrated over the area of the source:

$$\boldsymbol{\theta}_{cl}^{fs} = \frac{\sum_i \int_D d\mathbf{u} S(\mathbf{u}) \boldsymbol{\theta}_i(\mathbf{u}) \mu_i(\mathbf{u})}{\sum_i \int_D d\mathbf{u} S(\mathbf{u}) \mu_i(\mathbf{u})}, \quad (58)$$

where the sum is over all the microimages. The denominator is simply the total flux,  $\bar{S} \pi \rho_*^2 \mu_{tot}^{fs}$ . Again, for  $\theta_* \ll \theta_E$ , the centroid  $\boldsymbol{\theta}_0(\mathbf{u})$  of the images not associated with the fold varies slowly over the source. This yields  $\pi^{-1} \int_D d\mathbf{u}' S_N(\mathbf{u}') \mu_0(\mathbf{u}') \boldsymbol{\theta}_0(\mathbf{u}') = \mu_0(\mathbf{u}_{cn}) \boldsymbol{\theta}_0(\mathbf{u}_{cn})$  (since  $\mu_0(\mathbf{u})$  is also slowly varying over the source). Equation (58) then separates into two terms:

$$\boldsymbol{\theta}_{cl}^{fs} = \frac{\mu_f^{fs}}{\mu_{tot}^{fs}} \left[ \frac{1}{\pi \rho_*^2 \bar{S} \mu_f^{fs}} \int_D d\mathbf{u} S(\mathbf{u}) \boldsymbol{\theta}_f(\mathbf{u}) \mu_f(\mathbf{u}) \right] + \frac{\mu_{0,cn}}{\mu_{tot}^{fs}} \boldsymbol{\theta}_{0,cn} \quad (59)$$

$$= \frac{\mu_f^{fs}}{\mu_{tot}^{fs}} \boldsymbol{\theta}_f^{fs} + \frac{\mu_{0,cn}}{\mu_{tot}^{fs}} \boldsymbol{\theta}_{0,cn}, \quad (60)$$

where  $\boldsymbol{\theta}_{0,cn} \equiv \boldsymbol{\theta}_0(\mathbf{u}_{cn})$ . The first term in (60) is the contribution from the two images associated with the fold caustic, while the second term is the contribution from all unrelated images. For convenience, we defined  $\boldsymbol{\theta}_f^{fs}$  to be the factor within the brackets in equation (59).

The term  $\boldsymbol{\theta}_f^{fs}$  will now be evaluated. Since  $\mathbf{u} = \rho_* \mathbf{u}' + \mathbf{u}_{cn}$ , we obtain

$$\boldsymbol{\theta}_f(\mathbf{u}) = \boldsymbol{\theta}_f(\mathbf{u}_{cn}) + \rho_* \boldsymbol{\theta}_f(\mathbf{u}'). \quad (61)$$

Define  $\boldsymbol{\theta}_{f,cn} \equiv \boldsymbol{\theta}_f(\mathbf{u}_{cn}) \Theta(1+z)$ , so  $\boldsymbol{\theta}_{f,cn}$  vanishes when the disc source lies completely below the fold caustic.<sup>8</sup> Using (52), we find a simple formula for the finite source image centroid,

$$\boldsymbol{\theta}_f^{fs}(t) = \boldsymbol{\theta}_{f,cn} + \frac{\sqrt{u_f \rho_*}}{\mu_f^{fs}} \boldsymbol{\theta}_f(\mathcal{H}_{S_N}, \mathcal{K}_{S_N}), \quad (62)$$

where we have defined

$$\mathcal{H}_{S_N}(z) = \frac{1}{\pi} \int_{\max(-z, -1)}^1 du'_2 \frac{\Theta(1+z)}{\sqrt{u'_2 + z}} \int_{-\sqrt{1-(u'_2)^2}}^{\sqrt{1-(u'_2)^2}} du'_1 u'_1 S_N(u'_1, u'_2), \quad (63)$$

$$\mathcal{K}_{S_N}(z) = \frac{1}{\pi} \int_{\max(-z, -1)}^1 du'_2 u'_2 \frac{\Theta(1+z)}{\sqrt{u'_2 + z}} \int_{-\sqrt{1-(u'_2)^2}}^{\sqrt{1-(u'_2)^2}} du'_1 S_N(u'_1, u'_2). \quad (64)$$

---

<sup>8</sup>Technically, the fold produces no images locally of  $\mathbf{u}_{cn}$  when  $z < 0$ , and thus  $\boldsymbol{\theta}_f(\mathbf{u}_{cn})$  is not defined for  $z < 0$ . This apparent discrepancy can be alleviated by simply assuming that  $\boldsymbol{\theta}_f(u_1, u_2)$  is a function that is defined for all  $u_1, u_2$ , i.e.,  $\boldsymbol{\theta}_f(u_1, u_2) = (du_1 - bu_2, -bu_1)/(ad)$  for all  $u_1, u_2$ .



In the case of a uniform source, we obtain<sup>9</sup>  $\mathcal{H}_{S_N}(z) = 0$  and  $\mathcal{K}_{S_N} = \mathcal{K}_0$ , where

$$\mathcal{K}_n(z) \equiv \pi^{-1/2} \frac{(n+1)!}{(n+1/2)!} \int_{\max(-z, -1)}^1 dx x \frac{(1-x^2)^{n+1/2}}{(x+z)^{1/2}} \Theta(1+z). \quad (65)$$

For a uniform source, the finite source centroid of the two images associated with the fold is then,

$$\boldsymbol{\theta}_f^{us} = \boldsymbol{\theta}_{f,cn} - \frac{b \sqrt{u_f \rho_*}}{ad \mu_f^{fs}} \mathcal{K}_0(z) \hat{\mathbf{i}}, \quad (66)$$

where  $\hat{\mathbf{i}} \equiv (1, 0)$ . Inserting the definition of  $\mu_f^{us}$ , this can also be written in the alternate form,

$$\boldsymbol{\theta}_f^{us} = \boldsymbol{\theta}_{f,cn} - \frac{b \rho_* \mathcal{K}_0(z)}{ad G_0(z)} \hat{\mathbf{i}}. \quad (67)$$

Figure 2 shows the functions  $\mathcal{K}_0(z)$  and  $G_0(z)$ , while Figure 3 depicts  $\mathcal{K}_0(z)/G_0(z)$ . Figure 1(g) illustrates the behavior of the image centroid (Eq. 60) for a finite source.

### 2.3. Limb Darkening

In this section we consider the effect of non-uniform sources on the magnification and centroid shift near folds. The effect of generic surface brightnesses can be evaluated using the general integral forms for the magnification (Eq. 53), and the two components of the centroid shift (Eqs. 63 and 64). We will concentrate on a specific form for  $S(\mathbf{u})$  applicable to stellar sources, namely

$$S_N(\mathbf{u}) = \left\{ 1 - \Gamma \left[ 1 - \frac{3}{2} \left( 1 - \frac{|\mathbf{u} - \mathbf{u}_{cn}|^2}{\rho_*^2} \right)^{1/2} \right] \right\}, \quad (68)$$

where  $\mathbf{u}_{cn}$  is the center of the source. Here  $\Gamma$  is the limb darkening parameter, which may be wavelength dependent. This form was originally introduced by Albrow et al. (1999), and it has the desirable property that there is no net flux associated with the limb darkening term.

Inserting this form for the surface brightness into equation (53), we recover the result of Albrow et al. (1999) for the limb darkened magnification

$$\mu_f^{ld} = \mu_f^{us} + \Gamma \left( \frac{u_f}{\rho_*} \right)^{1/2} [G_{1/2}(z) - G_0(z)], \quad (69)$$

---

<sup>9</sup>In fact,  $\mathcal{H}_{S_N}(z) = 0$  for any profile with the symmetry  $S_N(u'_1, u'_2) = S_N(-u'_1, u'_2)$ .

where  $G_n(z)$  is defined in equation (55), and  $G_0(z)$ ,  $G_{1/2}(z)$ , and  $G_{1/2}(z) - G_0(z)$  are shown in Figure 2.

Since this form of the surface brightness profile is symmetric,  $S_N(u'_1, u'_2) = S_N(-u'_1, u'_2)$ , the integral  $\mathcal{H}_{S_N}$  vanishes. Inserting equation (68) into the general form for  $\mathcal{K}_{S_N}$ , we find  $\mathcal{K}_{S_N} = \mathcal{K}_0 + \Gamma(\mathcal{K}_{1/2} - \mathcal{K}_0)$ , and thus,

$$\boldsymbol{\theta}_f^{ld} = \boldsymbol{\theta}_{f,cn} - \frac{b \sqrt{u_f} \rho_*}{ad \mu_f^{ld}} [\mathcal{K}_0(z) + \Gamma(\mathcal{K}_{1/2} - \mathcal{K}_0)] \hat{\mathbf{i}}, \quad (70)$$

which can also be written,

$$\boldsymbol{\theta}_f^{ld} = \boldsymbol{\theta}_{f,cn} - \frac{b\rho_*}{ad} \left[ \frac{\mathcal{K}_0(z) + \Gamma(\mathcal{K}_{1/2} - \mathcal{K}_0)}{G_0(z) + \Gamma(G_{1/2} - G_0)} \right] \hat{\mathbf{i}}. \quad (71)$$

Figure 2 shows the functions  $\mathcal{K}_0(z)$ ,  $\mathcal{K}_{1/2}(z)$ , and  $\mathcal{K}_{1/2}(z) - \mathcal{K}_0(z)$ , while Figure 3 depicts the term in brackets above for several values of  $\Gamma$ .

## 2.4. Simple Linear Folds

The majority of the results presented in §2 (with the exception of the assumption made in §§2.2 and 2.3 that the caustic is coincident with the  $u_1$ -axis) are applicable for the general case of a parabolic fold catastrophe. In some cases, however, it is possible to simplify the expressions considerably and recover the more familiar linear fold form.

To see how this limit may be reached, consider the form for the general fold mapping in equation (11). In this form, the source and image plane coordinates have all been normalized by  $\theta_E$ , and thus are dimensionless, as are the coefficients  $a, b, c, d$  (since  $\psi$  is dimensionless). It is clear that the caustic will (in general) be appreciably curved when one considers order unity variations in  $u_1, u_2$  (i.e., on absolute angular scales of order  $\theta_E$ ). In other words, in the general case one can expect that all of the coefficients ( $a, b, c, d$ ) to be of the same order of magnitude. Now consider variations on some smaller scale  $\theta_\epsilon \ll \theta_E$ . Renormalizing the angular source and image plane variables such that  $\hat{\mathbf{u}} = (\theta_E/\theta_\epsilon)\mathbf{u}$  and  $\hat{\boldsymbol{\theta}} = (\theta_E/\theta_\epsilon)\boldsymbol{\theta}$ , the fold mapping can be recast in the form

$$\hat{u}_1 = A\hat{\theta}_1 + \frac{B}{2}\hat{\theta}_2^2 + C\hat{\theta}_1\hat{\theta}_2, \quad \hat{u}_2 = \frac{C}{2}\hat{\theta}_1^2 + B\hat{\theta}_1\hat{\theta}_2 + \frac{D}{2}\hat{\theta}_2^2, \quad (72)$$

where the relation between the coefficients are  $A = a$ ,  $B = b(\theta_\epsilon/\theta_E)$ ,  $C = c(\theta_\epsilon/\theta_E)$ , and  $D = d(\theta_\epsilon/\theta_E)$ . Therefore, on scales of order  $\theta_\epsilon$ , we can expect  $A$  to be larger than  $B, C$  and  $D$  by a factor  $\theta_E/\theta_\epsilon$ . In the Galactic microlensing case, for example, one is typically

concerned with variations on the scale of the source, i.e., scales of order  $\theta_\epsilon \approx \theta_*$ . In this case  $\theta_E/\theta_\epsilon \gtrsim 100$ .

Let us consider the curvature of the fold caustic on scales of  $\mathcal{O}(\theta_\epsilon)$ . In general, for a twice continuously differentiable function  $f = f(x)$  on an open interval of  $\mathbf{R}$ , the magnitude of the curvature at a point  $(x_0, f(x_0))$  on the graph of  $f$  is given by

$$|\hat{k}(x_0)| = \frac{f''(x_0)}{[1 + (f'(x_0))^2]^{3/2}}. \quad (73)$$

In the coordinates of (72), i.e. on scales of  $\mathcal{O}(\theta_\epsilon)$ , equation (18) yields that the fold caustic can be expressed as a graph  $(\hat{u}_1, f(\hat{u}_1))$ , where

$$f(\hat{u}_1) = \hat{e} \hat{u}_1^2, \quad \hat{e} \equiv \frac{CD - B^2}{2A^2D}. \quad (74)$$

By (73),

$$|\hat{k}(\hat{u}_1)| = \frac{2|\hat{e}|}{[1 + 4\hat{e}^2 \hat{u}_1^2]^{3/2}}. \quad (75)$$

But

$$\hat{e} = \left(\frac{\theta_\epsilon}{\theta_E}\right) e, \quad \hat{u}_1 = \left(\frac{\theta_E}{\theta_\epsilon}\right) u_1. \quad (76)$$

Hence, the magnitude of the curvature of the fold caustic can be expressed as

$$|\hat{k}(\hat{u}_1)| = \left(\frac{\theta_\epsilon}{\theta_E}\right) \frac{2|e|}{[1 + 4e^2 u_1^2]^{3/2}}. \quad (77)$$

Equation (77) yields that, at the origin and on scales comparable to  $\theta_\epsilon$ , the magnitude of curvature scales as  $\theta_\epsilon/\theta_E$ , and is given by  $|\hat{k}(0)| = 2(\theta_\epsilon/\theta_E)e$ . Note that the radius of curvature at the origin is  $|\hat{k}(0)|^{-1}$ . In Galactic microlensing  $\theta_\epsilon \sim \theta_*$  and  $\theta_*/\theta_E \ll 1$ . Therefore it is generally the case that  $|\hat{k}| \ll 1$ , i.e., the curvature of the fold caustic is negligible on scales of order  $\theta_*$ , and the fold can be treated as linear.

We therefore ask what happens to the expressions derived in the previous sections in the limit that  $a \gg (b, c, d)$ . We find that  $C(u_1, u_2) \simeq 2a^2 du_2$ , and thus the caustic, which is defined by  $C(u_1, u_2) = 0$ , collapses to the  $u_1$ -axis (linear fold). The critical curve is still given by  $\theta_2 = -(b/d)\theta_1$ . There are images whenever  $u_2 \geq 0$ , which are located at

$$\boldsymbol{\theta}_\pm = \left(\frac{u_1}{a}, \pm \sqrt{\frac{2u_2}{d}}\right), \quad (78)$$

with magnifications,

$$\mu_\pm = \frac{1}{2} \sqrt{\frac{u_f}{u_2}}. \quad (79)$$

The centroid of the two images therefore takes on the simple form,

$$\boldsymbol{\theta}_f = \left( \frac{u_1}{a}, 0 \right). \quad (80)$$

Including the additional images, and assuming a rectilinear trajectory, the total magnification can be written,

$$\mu_{tot}(t) = \left( \frac{t_f}{t - t_c} \right)^{1/2} \Theta(t - t_c) + \mu_{0,c} + \dot{\mu}_{(0,c)}(t - t_c), \quad (81)$$

The centroid of all the images has the same form as before (Eq. 48), with

$$\boldsymbol{\theta}_{f,c} = \left( \frac{u_{c,1}}{a}, 0 \right) \quad \dot{\boldsymbol{\theta}}_{(f,c)} = \left( \frac{\cos \phi}{at_E}, 0 \right). \quad (82)$$

For finite sources, the centroid in (66) reduces to  $\boldsymbol{\theta}_f^{fs} = \boldsymbol{\theta}_{f,cn}$ . The finite source centroid then becomes

$$\boldsymbol{\theta}_{cl}^{fs} = \frac{\mu_f^{fs}}{\mu_{tot}^{fs}} \boldsymbol{\theta}_{f,cn} + \frac{\mu_{0,cn}}{\mu_{tot}^{fs}} \boldsymbol{\theta}_{0,cn}, \quad (83)$$

This is the same result as for point sources (see Eq. 42) if the point source magnification is replaced with the finite source magnification.

Equations (78)-(83) should hold whenever (1)  $a \gg (b, c, d)$ , (2) one is not too close to a higher-order catastrophe, i.e., a cusp, and (3) there are no other nearby folds.

## 2.5. Some Applications

We can use the results from the previous sections to derive some generic results about the astrometric behavior near folds. We first consider the magnitude of the astrometric jump when the source crosses a caustic. It is clear that for a point source, the maximum centroid shift is  $\Delta\theta_{jump} \equiv |\boldsymbol{\theta}_{f,c} - \boldsymbol{\theta}_{0,c}|$ , where  $\boldsymbol{\theta}_{f,c}$  is the point on the critical curve where the images merge. Although  $\Delta\theta_{jump}$  ultimately depends on the source trajectory and the topology of the lens, we can typically expect that  $\Delta\theta_{jump}$  is  $\mathcal{O}(\theta_E)$ . For the finite source case, the difference between the centroid position just before ( $z \sim -1$ ) and just after ( $z \sim 1$ ) the caustic crossing is  $\Delta\theta_{jump}^{fs} \simeq (\mu_f^{fs} / \mu_{tot}^{fs}) \Delta\theta_{jump}$ . For a uniform source, this is

$$\Delta\theta_{jump}^{us} \simeq \left[ 1 + \sqrt{\frac{\rho_*}{u_f} \frac{\mu_{0,cn}}{G_0}} \right]^{-1} \Delta\theta_{jump}. \quad (84)$$

Adopting typical parameters,  $\mu_{0,cn} \sim 1$ ,  $u_f \sim 1$ , and  $G_0 \sim 1$ , we find the fractional change from the point source case to be  $(\Delta\theta_{jump}^{fs} - \Delta\theta_{jump})/\Delta\theta_{jump} \sim -3\%(\rho_*/10^{-3})^{1/2}$ .

We now consider the magnitude of limb darkening effect on the magnification and centroid shift relative to the uniform source case. From equations (56) and (69), the fractional difference between the limb-darkened and uniform-source magnification is,

$$\delta\mu_{ld} \equiv \frac{\mu_{tot}^{ld} - \mu_{tot}^{us}}{\mu_{tot}^{us}} = \Gamma \frac{G_{1/2} - G_0}{G_0} \left[ 1 + \sqrt{\frac{\rho_*}{u_f} \frac{\mu_{0,cn}}{G_0}} \right]^{-1}. \quad (85)$$

Early in the caustic crossing ( $z < 1$ ), the factor  $\sqrt{\rho_*/u_f}(\mu_{0,cn}/G_0)$  is small compared to unity, and thus  $\delta\mu_{ld} \sim \Gamma(G_{1/2} - G_0)/G_0$ . The magnitude of  $(G_{1/2} - G_0)/G_0$  is  $\leq 20\%$  for the majority ( $z \lesssim 0.8$ ) of the caustic crossing. Near the end of the caustic crossing ( $z \sim 1$ ) the term in brackets begins to dominate as  $G_0 \rightarrow 0$ , and thus  $\delta\mu_{ld} \sim \Gamma\mu_{0,cn}^{-1}\sqrt{u_f/\rho_*}(G_{1/2} - G_0)$ , which goes to zero as  $z \rightarrow 1$ . Thus for typical values of  $u_f$ ,  $\rho_*$ , and  $\mu_{0,cn}$ , the fractional difference from a uniform source is  $\lesssim 0.2\Gamma$  for the majority of the caustic crossing. See Figure 3.

The difference in the centroid due to limb darkening is

$$\Delta\theta_{cl}^{ld} = \theta_{cl}^{ld} - \theta_{cl}^{us} = \delta\mu_{ld} \frac{\mu_{0,cn}}{\mu_{tot}^{ld}} (\theta_f - \theta_0). \quad (86)$$

Figure 3(c) shows the prefactor  $\delta\mu_{ld}\mu_{0,cn}/\mu_{tot}^{ld}$  for  $\mu_{0,cn} = 4$ ,  $u_f = 1$ , and several values of  $\rho_*$ . To assess the detectability of the deviation of the centroid shift from the uniform source case due to limb darkening in Galactic bulge microlensing events, we now make a crude estimate for the maximum magnitude of  $\Delta\theta_{cl}^{ld}$  by adopting typical parameters. At  $t = t_c$ , we have that  $|\theta_f - \theta_0| = \Delta\theta_{jump}$ , and is maximized. We will assume that  $\Delta\theta_{jump} \sim \theta_E \sim 300\mu\text{as}$ . We have just argued that  $\delta\mu_{ld} \lesssim 0.2\Gamma$ . Near the end of the caustic crossing (where  $\delta\mu_{ld}$  is maximized),  $\mu_{tot}^{ld} \sim \mu_0$ . Inserting these values into equation (86), we find

$$|\Delta\theta_{cl}^{ld}|_{max} \sim (60\Gamma) \mu\text{as}. \quad (\text{Bulge Lenses}). \quad (87)$$

For typical values of  $\Gamma \sim 0.5$  in the optical,  $|\Delta\theta_{cl}^{ld}|_{max} \lesssim 30\mu\text{as}$ , which is only a factor of  $\sim 3-6$  larger than the sensitivity expected from *SIM*. Note that this is the *maximum* centroid shift; inspection of Figure 3(c) reveals that  $|\Delta\theta_{cl}^{ld}|$  is considerably smaller than this maximum for the majority of the caustic crossing. Therefore, detection of the astrometric effects of limb-darkening will likely be challenging, at least for Galactic bulge lensing events, with the currently planned accuracy for *SIM*. On the other hand, the fact that the astrometric effects of limb darkening are small implies that limb-darkening can generally be ignored. Thus predictions for the signatures of other effects, such as the finite source effect itself, are

robust. In other words, measurements generally should not be compromised by an unknown amount of limb-darkening.

Consider two observers that are not spatially coincident. The source trajectories as seen by the two observers will be displaced relative to each other by an amount  $\delta\mathbf{u}$ , the magnitude of which is  $|\delta\mathbf{u}| = a_{\oplus s}/\tilde{r}_E$ , where  $a_{\oplus s}$  is the component of the separation between the two observers perpendicular to the line-of-sight, and  $\tilde{r}_E = \theta_E D$  is the Einstein ring radius projected to the observer plane. If  $\delta\mathbf{u}$  is sufficiently large, then both the photometric and astrometric behavior of the event will be measurably different between the two observers, an effect commonly known as parallax. Since  $a_{\oplus s}$  is known, this observed difference can be used to infer  $\tilde{r}_E$ , providing additional physical constraints on the properties of the lens. For example, when combined with a measurement of  $\theta_E$  from the astrometric centroid shift itself, the mass of the lens can be determined,  $M = (c^2/4G)\tilde{r}_E\theta_E$ . For a given  $|\delta\mathbf{u}|$ , parallax effects are typically largest near caustics, because the magnification and the centroid vary rapidly with respect to source position. Thus caustic crossings are ideal for use in measuring parallax effects (Hardy & Walker 1995; Gould & Andronov 1999). If  $|\delta\mathbf{u}|$  is sufficiently small that the behavior near the fold caustic crossing for both observers can be described by the same local expansion of the lens mapping, then the results derived here can be used to fit the astrometric and photometric behavior for both observers and derive the parallax effects without regard to the global behavior of the lens. We note that, for generic fold caustics, any significant displacement  $\delta\mathbf{u}$ , regardless of its orientation relative to the caustic, will result in a difference in the observable behavior. However, for linear fold caustics (§2.4), only displacements perpendicular to the caustic will result in significant differences in the magnification and centroid. Thus, for generic linear fold caustics, only a projection of  $\tilde{r}_E$  is measurable from the local caustic behavior (Graff & Gould 2002).

During a fold caustic crossing the source is resolved, altering both the photometric and astrometric behavior with respect to a point source (§2.2). The photometric behavior near a caustic crossing depends on  $\rho_*$ , the source size in units of  $\theta_E$ , whereas the astrometric behavior depends on actual angular size of the source  $\theta_* = \rho_*\theta_E$ .<sup>10</sup> Thus, while fitting to the photometric data near a caustic crossing does not yield the angular size of the source, fitting to the astrometric data near a caustic crossing does. Therefore it is possible, in principle, to measure the angular radius of the source star of a caustic-crossing binary-lens event by fitting a few astrometric measurements taken during the caustic crossing to the expressions we have derived for the local astrometric behavior (see §2.2.2 and Eq. 60). In practice, however, this is complicated by the fact that, for linear fold caustics, only the degenerate

---

<sup>10</sup>Recall that, in order to convert to astrometric observables, all angular variables must be multiplied by  $\theta_E$ .

combination  $\theta_*/\sin\phi$  can be measured, where  $\phi$  is the angle of the trajectory with respect to the caustic. For general fold caustics, the degeneracy between  $\theta_*$  and  $\sin\phi$  is broken (see §2.2.2 and Eq. 67), however, for many cases the simple linear fold will be applicable. Thus, in order to determine  $\theta_*$  separately, the global geometry must be generally specified, which can be accomplished using the global photometric light curve.

### 3. A Worked Example: Binary Lensing Event OGLE-1999-BUL-23

In this section we numerically calculate the expected astrometric behavior for a binary-lens fold caustic crossing, and compare this with the analytic results from the previous sections. We do this in order to verify our expressions and also to explore the accuracy with which our (necessarily) approximate results reproduce the exact behavior. For definiteness, we will calculate the expected astrometric behavior for the photometrically well-observed caustic-crossing binary lens event OGLE-1999-BUL-23 (Albrow et al. 2001). This has the advantage that, up to an orientation on the sky and subject to small errors in the inferred parameters, the astrometric behavior can be essentially completely determined from the photometric solution, including the size of  $\theta_E$  and the effects of limb-darkening.

#### 3.1. Formalism and Procedures

For a system of  $N_l$  point masses located at positions  $\boldsymbol{\theta}_{l,j}$ , and no external shear, the lens equation (Eq. 3) takes the form

$$\mathbf{u} = \boldsymbol{\theta} - \sum_{j=1}^{N_l} m_j \frac{\boldsymbol{\theta} - \boldsymbol{\theta}_{l,j}}{|\boldsymbol{\theta} - \boldsymbol{\theta}_{l,j}|^2}, \quad (88)$$

where  $m_j$  is the mass of the  $j$ -th lens in units of the total mass. Note that angles in equation (88) are normalized to the  $\theta_E$  for the total mass of the system. For  $N_l = 2$ , the lens equation is equivalent to a fifth-order polynomial in  $\boldsymbol{\theta}$ , thus yielding a maximum of five images. All of the image positions for a given point on the source plane can be found numerically using any standard root finding algorithm. Then the individual magnifications, total magnification and centroid of these images can be found using equations (6), (8), and (9).

For a finite source size, it is necessary to integrate over the area of the source (Eq. 49). This can be difficult to do numerically in the source plane near the caustics, due to the divergent magnification. A more robust method is inverse ray shooting. This works as

follows. The image plane is sampled uniformly and densely, and at each  $\boldsymbol{\theta}$ , equation (88) is used to find the corresponding  $\mathbf{u}(\boldsymbol{\theta})$ . The local ratio of the density of rays in  $\boldsymbol{\theta}$  to the density of rays in  $\mathbf{u}$  is the local magnification. Thus one can create a map of  $\mu(\mathbf{u})$ , the magnification as a function of  $\mathbf{u}$ . Similarly, one can determine the astrometric deviation by sampling in  $\boldsymbol{\theta}$ , using equation (88) to determine  $\mathbf{u}(\boldsymbol{\theta})$ , and then summing at each  $\mathbf{u}$  the values of  $\boldsymbol{\theta}(\mathbf{u})$ . The astrometric deviation at  $\mathbf{u}$  is then the summed values of  $\boldsymbol{\theta}(\mathbf{u})$ , weighted by the local magnification. Thus one creates two astrometric maps, for each direction. In practice, inverse ray shooting requires one to bin the rays in the source plane, with the resolution of the maps being determined by the size of the bin, and the accuracy determined by surface density of rays in the image plane relative to the (unlensed) surface density of rays in the source plane. The advantage of inverse ray shooting is that the procedure conserves flux, therefore the maps can be convolved with any source profile to produce the finite source photometric and astrometric behavior for arbitrary source size and surface brightness profile.

To apply this method to predict the detailed photometric and astrometric behavior of the caustic crossings for OGLE-1999-BUL-23, it is essential that the resolution of the astrometric and photometric maps be considerably smaller than the source size  $\rho_*$ . We will be using resolutions of  $10^{-4}\theta_E$ , which corresponds to  $0.034\rho_*$  for OGLE-1999-BUL-23. This is sufficient to accurately resolve the source. We sample the image plane with a density of  $5 \times 10^9\theta_E^{-2}$ , corresponding to an Poisson error per resolution element of  $\sim 14\%\mu^{-1}$ . Since there are  $\sim 2700$  resolution elements per source size, the total Poisson error is always  $< 1\%$ , considerably smaller than any of the effects we will be considering.

### 3.2. Global Astrometric Behavior

Before studying the detailed behavior near the photometrically well-covered (second) caustic crossing of OGLE-1999-BUL-23, we first analyze the global astrometric behavior of the entire event. We specify the binary-lens topology and source trajectory using the parameters of the best-fit solution with limb darkening (see Table 2 of Albrow et al. 2001). In Figure 4 we show various aspects of the inferred lensing system and the event itself. The best-fit lens system has a wide topology, with two well-separated caustic curves, one near the position of each lens. The mass ratio of the two lenses is  $q \equiv m_1/m_2 = 0.39$ , and they are separated by  $2.42\theta_E$ . The solution has the source crossing the caustic associated with the least massive lens, which we will call the secondary caustic.

Figure 4(a) shows the photometric light curve centered on the event. There are two fold caustic crossings, separated by  $\sim 10$  days; the second crossing was densely covered photometrically by Albrow et al. (2001), allowing them to determine not only the source



size  $\rho_*$ , but also limb-darkening coefficients  $\Gamma$  in each of two different photometric bands:  $\Gamma_I = 0.534$  ( $I$ -band) and  $\Gamma_V = 0.711$  ( $V$ -band). This allows us to predict the astrometric behavior including finite source and limb-darkening effects. Furthermore, by combining a measurement of  $\rho_* \equiv \theta_*/\theta_E$ , with a determination of the angular size of the source  $\theta_*$  from its color and magnitude, Albrow et al. (2001) measured the angular Einstein ring radius of the lens to be  $\theta_E = (634 \pm 43)\mu\text{as}$ . Therefore we can determine the absolute scale of the astrometric features and assess their detectability by comparing them with the expected accuracy of upcoming interferometers.

Figure 4(b) shows the caustics and critical curves, as well as the trajectory of the images of the source. One image is always near the most massive lens; this image has little effect on the resulting astrometric deviation other than a small net offset along the binary axis. Figure 4(c) shows a close-up of the region near the secondary caustic, along with the image centroid  $\boldsymbol{\theta}_{cl}$ . The components parallel and perpendicular to the binary axis are shown in Figures 4(e,d). Finally, Figure 4(f) shows  $\delta\boldsymbol{\theta}_{cl}$ , the centroid relative to the unlensed source position  $\boldsymbol{u}$ . In Figures 4(c-f), the large,  $\mathcal{O}(\theta_E)$  jumps that occur when the source crosses the caustic are evident.

### 3.3. The Second Fold Crossing

We now focus on the photometric and astrometric behavior near the second caustic crossing for OGLE-1999-BUL-23. In Figure 5(a) we show the caustic geometry and source trajectory near this crossing. The source passed  $\sim 0.02$  mas from a cusp. On the scale of the source size,  $\theta_* = 1.86\mu\text{as}$ , the curvature of the caustic can be neglected.

In Figure 5 we show the behavior near the second caustic crossing. Figure 5(c) shows the photometric behavior for two days centered on the caustic crossing, for the assumption of a uniform source, and a limb-darkened source with surface brightness profile given in equation (68), with  $\Gamma_I = 0.534$  and  $\Gamma_V = 0.711$ . Note the similarity of the shapes of the uniform source and limb-darkened light curves with the analytic forms  $G_0$  and  $G_{1/2}$  presented in Figure 2(a). We show our prediction for the astrometric behavior as a function of time for the components parallel and perpendicular to the binary axis in Figures 5(d) and (e), respectively [compare with Figure 1(e,f)]. We show both the instantaneous discontinuous jumps for a point-source centroid, along with the continuous centroid curves for finite sources. The limb-darkened and uniform source astrometric curves are extremely similar. In Figure 5(f) we show the predicted total astrometric behavior for the same time span. Notice how well the form of Figure 5(f) compares with Figure 1(g), which was obtained from our analytic forms. Figure 6 shows the same curve as Figure 5(f), except we have rotated the axes by

$\sim 55^\circ$ , shifted the origin to the image of the caustic crossing, and stretched the axes for visibility. In Figure 6, notice how the predicted shaped for the finite source centroids are smoothly rounded off near the bottom and has a sharp turn near the top.

Although the difference between the finite source and point source curves is quite substantial, the difference between the uniform source and limb darkened sources is very small. This is more clearly illustrated in Figure 7(a,b), where we show the two components of this difference,  $\Delta\theta_{cl}^{ld} = \theta_{cl}^{ld} - \theta_{cl}^{us}$ , for about four source radius crossing times centered on the crossing, i.e.  $|z| < 2$ . The form of  $\Delta\theta_{cl}^{ld}$  is very similar to the analytic expectation [see Eq. 86 and Figure 3(c)]. Furthermore, the two components of  $\Delta\theta_{cl}^{ld}$  are essentially perfectly (anti-) correlated, implying that the difference is essentially one-dimensional. This can be seen best in Figure 7(c), where we plot  $\Delta\theta_{cl,1}^{ld}$  versus  $\Delta\theta_{cl,2}^{ld}$ . Panel (d) is the same as panel (c), except we have rotated and stretched the axes. The maximum deviation is  $\sim (60\Gamma)\mu\text{as}$ , in satisfying agreement with the rough expectation (Eq. 87).

#### 4. Summary and Conclusion

We have presented a detailed study of gravitational lensing near fold catastrophes, concentrating on the regime where the individual images are unresolved, i.e. microlensing. By Taylor expanding the scalar potential  $\psi$  in the neighborhood of a fold up to third order in the image position, one can obtain a generic form for the lensing map near a fold. Beginning with this mapping, we derive the local lensing properties of a source in the vicinity of the fold caustic. Approximating the critical curve by its tangent line at the origin, we find that the caustic is locally a parabola. On one side of the parabola, the fold lenses a nearby source into two images; on the other side of the parabola, there are no images. We derive the image positions and magnifications as a function of the position of the source. We find that the magnifications of the two images are equal, and recover the well-known result that the magnification is inversely proportional to the square root of the distance to the caustic. We show how this holds for parabolic caustics (as well as linear caustics), provided that the ‘vertical’ distance from the caustic is used.

Assuming a rectilinear source trajectory, and allowing for the existence of slowly- and smoothly-varying images not associated with the fold caustic, we derive analytic expressions for the total magnification and image centroid (center-of-light) as a function of time.

We then consider how the photometric and astrometric behavior is altered in the presence of a finite source size. We derive semi-analytic expressions for the magnification and centroid as a function of time for both a uniform source, and limb-darkened source. Along

the way we derived expressions that can be used to evaluate the photometric and astrometric behavior near a fold for a source with arbitrary surface brightness profile.

We then show how and under what conditions the generic parabolic fold reduces to the more familiar linear fold. We derive simplified expressions for the individual and total image positions and magnifications near a linear fold.

We used some of our analytic results to derive a few generic properties of microlensing near folds. In particular, we derive and evaluate expressions for the magnitude of the centroid jump that occurs when a finite source crosses a fold relative to the point source jump, and the magnitude of the effect of limb darkening on both the photometric and astrometric behavior. Notably, we predict, for Galactic bulge lensing events, the shape of the centroid due to finite sources with uniform and limb darkening surface brightness profiles. We also find for Galactic bulge lensing that the effect of limb darkening on the image centroid near a fold is quite similar to the uniform source case, making the limb darkening effect difficult to detect by the currently planned accuracy for the instrumentation of *SIM*. We discussed how our formulae can be used to fit both photometric and astrometric data sets near fold caustic crossings and thus used to derive such properties as the angular size of the source and the microlensing parallax.

Finally, we numerically calculate expected astrometric behavior of the photometrically well-observed Galactic bulge binary lensing event OGLE-1999-BUL-23 (Albrow et al. 2001), finding excellent agreement with our analytic predictions.

Caustics are ubiquitous in gravitational lenses, and the most common type of caustic is the fold. Caustics play an especially important role in microlensing, as the rapid time variability of the total image magnification allows the possibility of detailed studies of the source and lens. In the future, we can expect that time-series photometric measurements will be supplemented by time-series *astrometric* measurements of the center-of-light of microlens systems. This paper presents the most thorough and comprehensive study of the photometric and astrometric behavior of gravitational microlensing near fold caustics to date. The results should prove useful to those studying microlens systems with caustics: The analytic expressions derived here can be used to fit fold caustic crossings observed both photometrically and astrometrically, gain some insight into more complicated numerical studies, and establish predictions for the feasibility of future observations.

We would like to thank the referee, Eric Agol, for several helpful suggestions that led to a much improved manuscript. B.S.G. was supported in part by NASA through a Hubble Fellowship grant from the Space Telescope Science Institute, which is operated by the Association of Universities for Research in Astronomy, Inc., under NASA contract NAS5-26555.

A.O.P. was supported in part by an Alfred P. Sloan Research fellowship and NSF Career grant DMS-98-96274.

## REFERENCES

- Albrow, M., et al. 1999b, *ApJ*, 522, 1022
- Albrow, M., et al. 2001, *ApJ*, 549, 759
- Alcock, C., et al. 2000, *ApJ*, 541, 270
- Boden, A.F., Shao, M., & van Buren, D. 1998, *ApJ*, 502, 538
- Chang, K. & Refsdal, S. 1979, *Nature*, 282, 561
- Chang, K., & Han, C. 1999, *ApJ*, 525, 434
- Corrigan, R. T. et al. 1991, *AJ*, 102, 34
- Fluke, C. J. & Webster, R. L. 1999, *MNRAS*, 302, 68
- Gaudi, B. S., & Gould, A. 1999, *ApJ*, 513, 619
- Gaudi, B.S., Graff, D.S., & Han, C. 2002, in preparation
- Gould, A. 1996, *PASP*, 108, 465
- Gould, A. 2000, *ApJ*, 535, 928
- Gould, A. 2001, *PASP*, 113, 903
- Gould, A. & Andronov, N. 1999, *ApJ*, 516, 236.
- Gould, A., & Han, C. 2000, 538, 653
- Gould, A., & Salim, S. 1999, *ApJ*, 524, 794
- Graff, D.S., & Gould, A. 2002, *ApJ*, submitted (astro-ph/0203313)
- Han, C., Chun, M.-S., & Chang, K. 1999, *ApJ*, 526, 405
- Hardy, S. J. & Walker, M. A. 1995, *MNRAS*, 276, L79.
- Irwin, M. J., Webster, R. L., Hewett, P. C., Corrigan, R. T., & Jędrzejewski, R. I. 1989, *AJ*, 98, 1989

- Jaroszyński, M., & Mao, S. 2001, MNRAS, 325, 1546
- Jeong, Y., Han, C., & Park, S.-H. 1999, ApJ, 511, 569
- Koopmans, L. V. E. & de Bruyn, A. G. 2000, A&A, 358, 793
- Lewis, G. F. & Belle, K. E. 1998, MNRAS, 297, 69
- Lewis, G. F. & Ibata, R. A. 1998, ApJ, 501, 478
- Mao, S., & Paczyński, B. 1991, ApJ, 374, 37
- Paczyński, B. 1986, ApJ, 304, 1
- Paczyński, B. 1995, Acta Astron., 45, 345
- Paczyński, B. 1998, ApJ, 494, L23
- Paczynski, B. 1996, ARA&A, 34, 419
- Petters, A. O., Levine, H., & Wambsganss, J. 2001, Singularity Theory and Gravitational Lensing (Boston: Birkhäuser).
- Schneider, P., Ehlers, J., & Falco, E. E. 1992, Gravitational Lenses (Berlin: Springer).
- Schneider, P., and Weiss A., 1992, A&A, 260,1
- Schmidt, R. & Wambsganss, J. 1998, A&A, 335, 379
- Udalski, A., et al. 2000, Acta Astron., 50, 1
- Wambsganss, J. 2001, in ASP 237: Gravitational Lensing: Recent Progress and Future Goals, eds. T. Brainerd and C.S. Kochanek. (San Francisco: ASP), 185
- Wambsganss, J. & Paczynski, B. 1991, AJ, 102, 864
- Wambsganss, J., Schneider, P., & Paczynski, B. 1990, ApJ, 358, L33
- Walker, M.A. 1995, ApJ, 453, 37
- Williams, L. L. R. & Saha, P. 1995, AJ, 110, 1471
- Witt, H. 1990, A&A, 236, 311
- Woźniak, P. R., Udalski, A., Szymański, M., Kubiak, M., Pietrzyński, G., Soszyński, I., & Żebruń, K. 2000, ApJ, 540, L65

Wyithe, J. S. B. & Webster, R. L. 1999, MNRAS, 306, 223

Wyithe, J. S. B., Webster, R. L., & Turner, E. L. 2000, MNRAS, 315, 51

Wyithe, J. S. B., Webster, R. L., Turner, E. L., & Mortlock, D. J. 2000, MNRAS, 315, 62

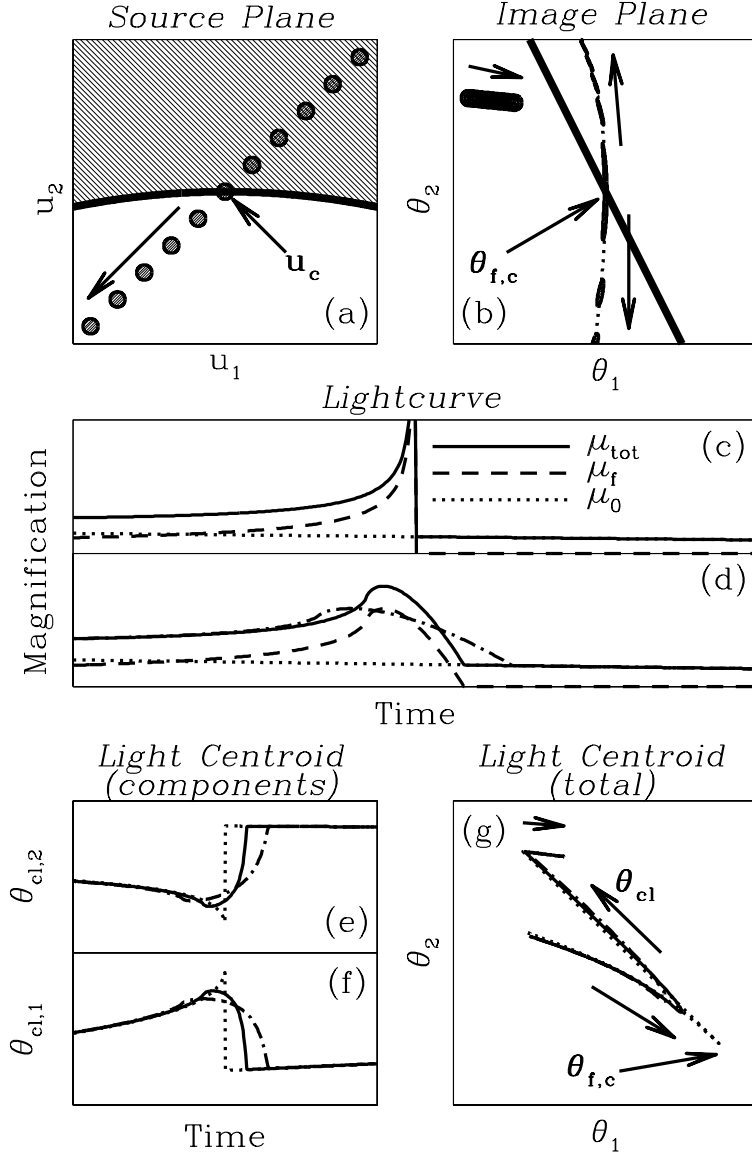


Fig. 1.— An illustration of the basic properties of astrometric and photometric microlensing near folds. (a) Filled circles represent the source at various times. The solid line is the fold. The source crosses the caustic at  $\mathbf{u}_c$ . (b) The elongated shapes are the images corresponding to the source at the positions in panel (a). The point  $\boldsymbol{\theta}_{f,c}$  is the image of  $\mathbf{u}_c$ , and is where the two extra images appear. The third image on the nearly horizontal trajectory represents the centroid of all images unassociated with the fold. (c) The magnification as a function of time for a point source. The solid line is the total magnification  $\mu_{tot}$ , the dotted line is the magnification of all images unassociated with the caustic  $\mu_0$ , and the dashed line is the magnification  $\mu_f$  of the two images created in the fold crossing. (d) Same as (c), except for a finite uniform source. The dashed-dot line shows the total magnification for a source size that is two times larger. (e) The  $\theta_{cl,1}$ -component of the centroid shift as a function of time. Dotted line is for a point-source, solid line for a finite uniform source size. Dashed-dot line is for a source size that is two times larger. (f) The  $\theta_{cl,2}$ -component of the centroid shift. (g) The path of the centroid of light of all the images,  $\boldsymbol{\theta}_{cl}$ . Line types are as in panels (e,f).

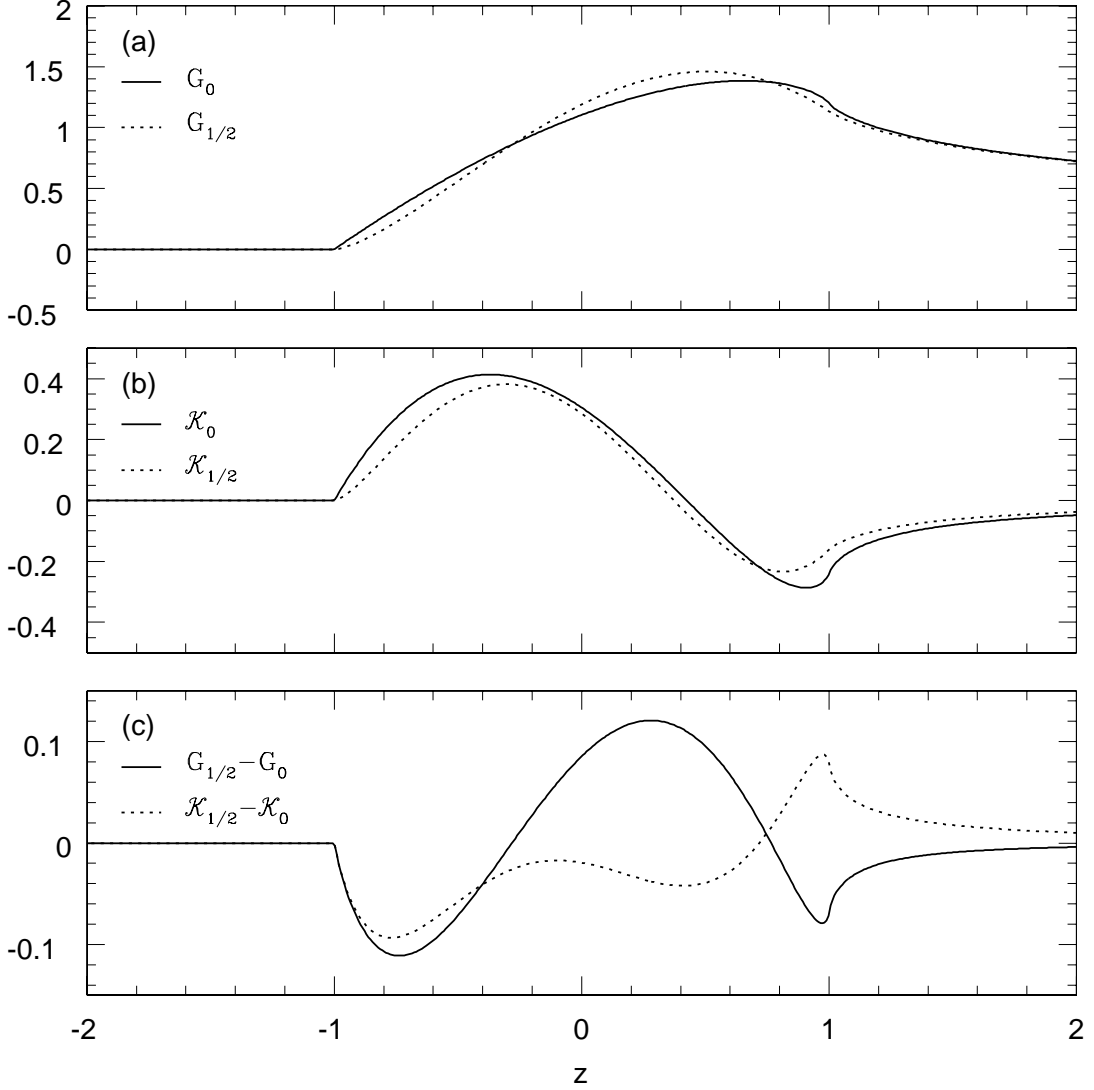


Fig. 2.— Basic functions which describe the photometric and astrometric behavior of finite sources near a fold, as a function of the distance  $z$  from the fold in units of the dimensionless source size  $\rho_*$ . (a) The basic functions for the photometric behavior. The solid line shows  $G_0$ , whereas the dotted line shows  $G_{1/2}$ . (b) The basic functions for the astrometric behavior. The solid line shows  $\mathcal{K}_0$ , whereas the dotted line shows  $\mathcal{K}_{1/2}$ . (c) The photometric ( $G_{1/2} - G_0$ ) and astrometric ( $\mathcal{K}_{1/2} - \mathcal{K}_0$ ) limb darkening functions. See text.



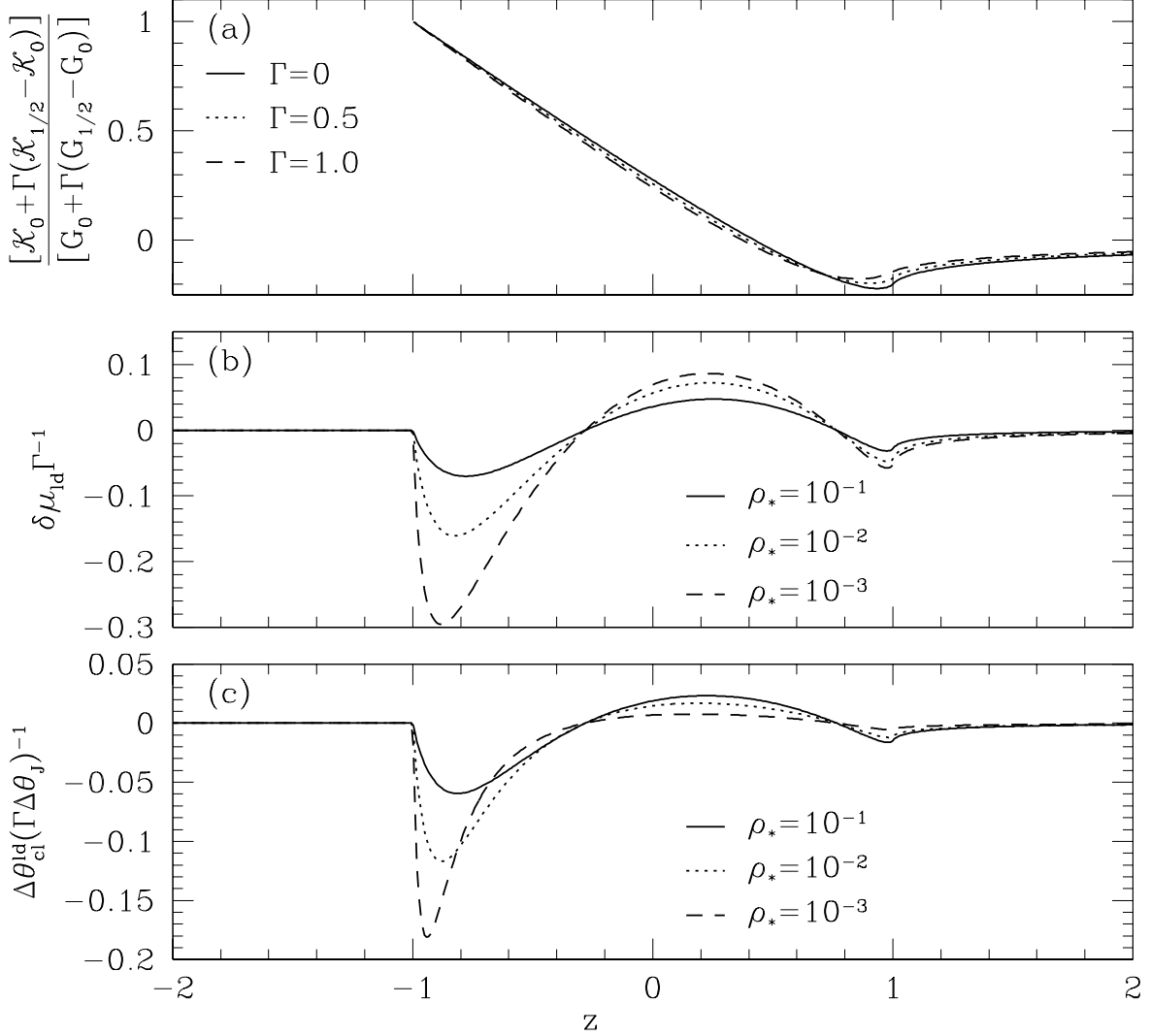


Fig. 3.— (a) The function  $[\mathcal{K}_0 + \Gamma(\mathcal{K}_{1/2} - \mathcal{K}_0)]/[G_0 + \Gamma(G_{1/2} - G_0)]$  as a function of  $z$ , for  $\Gamma = 0, 0.5$ , and  $1.0$ , where  $G_0$ ,  $G_{1/2}$ ,  $\mathcal{K}_0$ , and  $\mathcal{K}_{1/2}$  are shown in Figure 2, and  $\Gamma$  is a limb-darkening parameter. (b) The fractional difference  $\delta\mu_{ld}$  between the limb-darkened and uniform source magnifications, normalized by  $\Gamma$ , for several source sizes  $\rho_*$ . We have assumed a caustic scale  $u_f = 1$ , and magnification outside the caustic of  $\mu_{0, cn} = 4$ . (c) The absolute magnitude of the difference in the centroid shift due to limb darkening  $\Delta\theta_{cl}^{ld}$ , normalized by  $\Gamma\Delta\theta_{jump}$ , where  $\Delta\theta_{jump}$  is magnitude of the point-source astrometric ‘jump’ when the source crosses the caustic. See text.

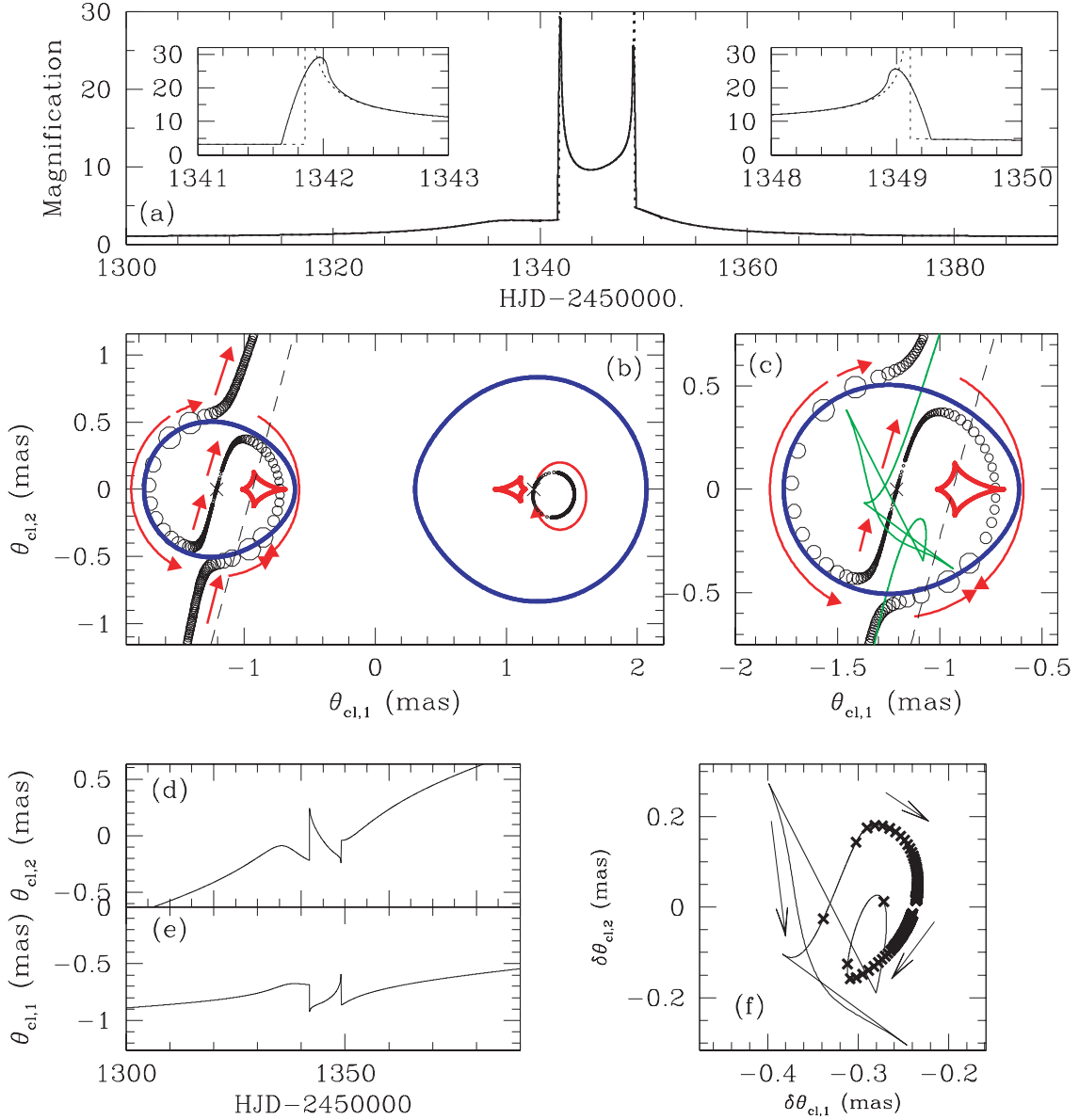


Fig. 4.— Global photometric and astrometric behavior of the binary-lens event OGLE-1999-BUL-23. (a) The light curve (magnification as a function of time) for the best-fit model. Solid line is for the finite source, whereas the dotted line is for a point source. The insets show detail near the two caustic crossings. (b) The critical curves (blue ovals), caustics (red cuspy curves), images (circles), and source trajectory (dashed line). The X’s denote the position of the two masses, the arrows give the directions of motion of the images, and the size of the circles are proportional to the magnification of the image. (c) Detail near the caustic crossing. The green lines shows the position of the centroid  $\theta_{cl}$  of the five images relative to the lens. (d,e) the two components of  $\theta_{cl}$  as a function of time. (f) The solid line shows the centroid relative to the source position  $\delta\theta_{cl}$ . The X’s show  $\delta\theta_{cl}$  at fixed intervals of 20 days.

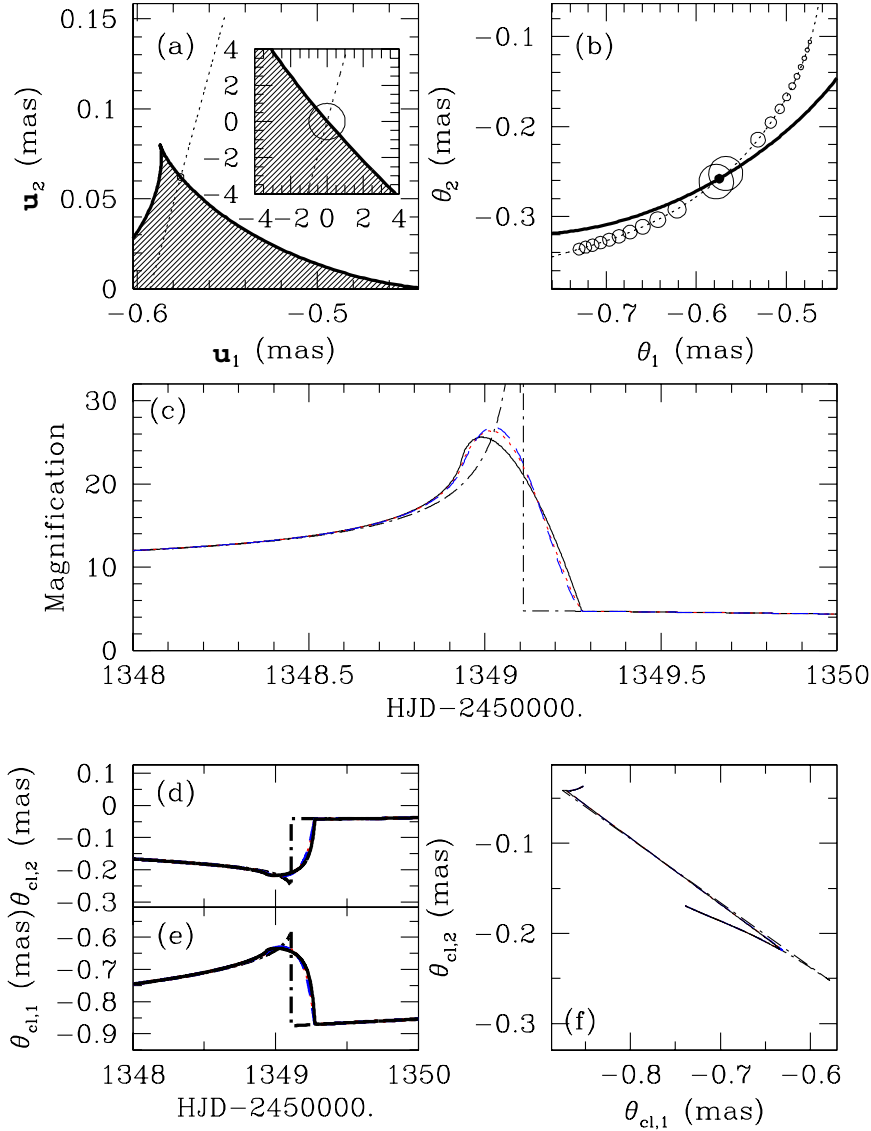


Fig. 5.— The photometric and astrometric behavior near the second caustic crossing of OGLE-1999-BUL-23. (a) The heavy solid line shows the caustic, while the dashed line shows the source trajectory. The interior of the caustic is shaded. The inset shows the detail near the caustic crossing, in units of the source size, shown as a circle. (b) The heavy solid line is the critical curve, and the circles show the positions of the two images associated with the caustic crossing at fixed intervals of 4.8 hours. The size of the circles is proportional to the logarithm of the magnification. (c) The magnification near the second caustic crossing as a function of time. The solid lines is for a uniform source, dotted line for a limb-darkened source in the  $I$ -band, dashed line for the  $V$ -band, and dashed-dot line is for a point source. (d,e) The two components of the centroid  $\theta_{cl}$  in mas as a function of time. Line types are the same as (c). (f) The centroid  $\theta_{cl}$ .

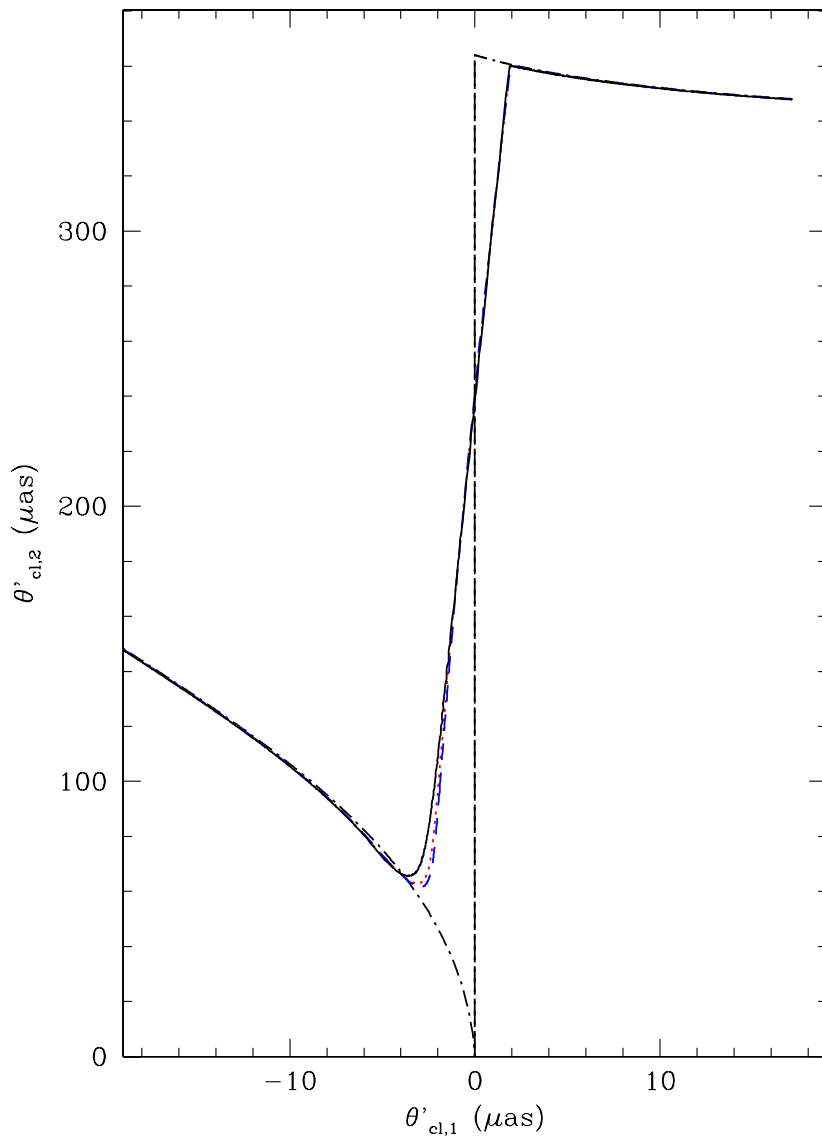


Fig. 6.— Detail of the centroid shift  $\theta_{cl}$  near the second caustic crossing of OGLE-1999-BUL-23 in  $\mu\text{as}$ . This is the same as panel (f) in Figure 5, except the axes have been rotated by  $\sim 55^\circ$ , and the origin has been translated to the image position of the caustic crossing point. Note the extreme asymmetry in the scales of the two axes. The solid line is for a uniform source, dotted line for a limb-darkened source in the  $I$ -band, dashed line for the  $V$ -band, and dashed-dot line is for a point source.

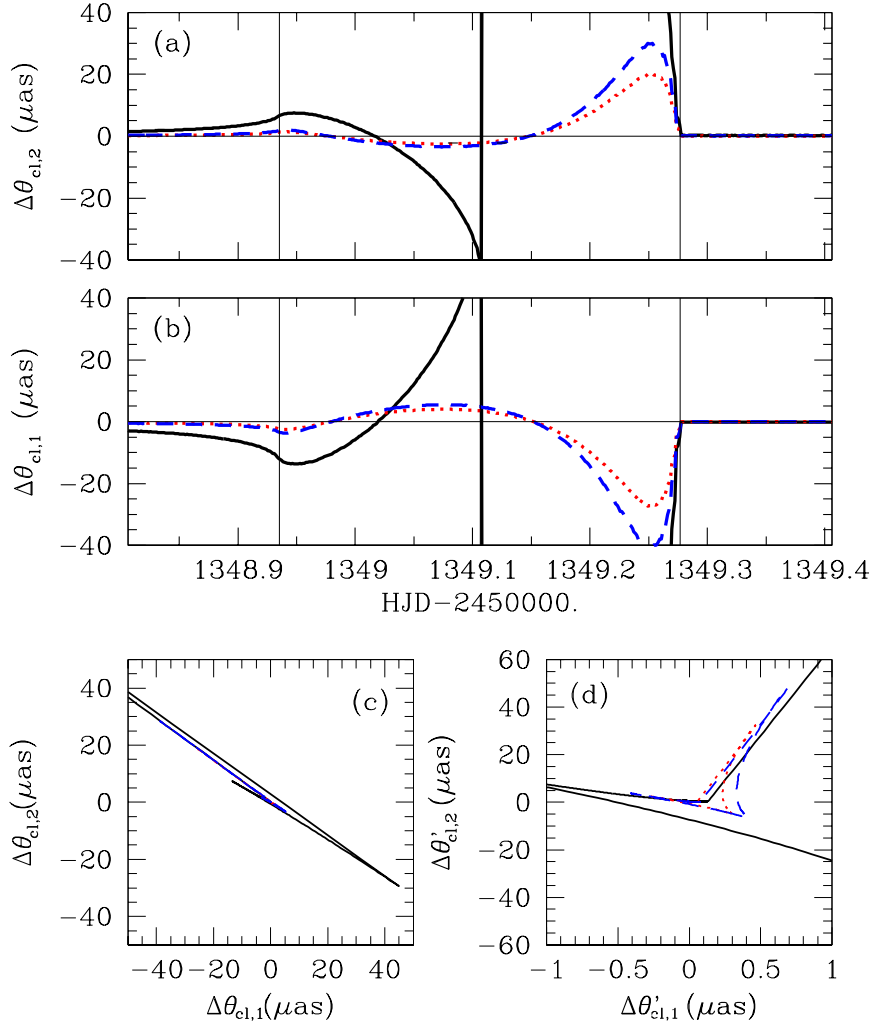


Fig. 7.— (a,b) The two components of the astrometric offset due to limb darkening  $\Delta\theta_{cl}^{ld}$  relative to a uniform source as a function of time. The dotted red line is for the  $I$ -band, where as the dashed line is for the  $V$ -band. The two components are parallel (a) and perpendicular (b) to the binary axis. The vertical lines show (from left to right) the time when the source first touches, straddles, and last touches the caustic. The solid lines is the offset from a point source. (c) The astrometric offset  $\Delta\theta_{cl}^{ld}$ . Line types are as in panels (a) and (b). The deviations from the uniform source are essentially one-dimensional. (d) The same as panel (c), except that the axes have been scaled and rotated by  $\sim 55^\circ$ . Note the extreme asymmetry in the scales of the axes. The maximum absolute deviation due to limb darkening is small,  $\lesssim 50\mu\text{as}$ .